

Submitted to Astrophysical Journal

Magnetohydrodynamic Simulations of A Rotating Massive Star Collapsing to A Black Hole

Shin-ichirou Fujimoto¹, Kei Kotake², Shoichi Yamada^{2,3}, Masa-aki Hashimoto⁴, and Katsuhiko Sato^{5,6}

ABSTRACT

We perform two-dimensional, axisymmetric, magnetohydrodynamic simulations of the collapse of a rotating star of $40 M_{\odot}$ and in the light of the collapsar model of gamma-ray burst. Considering two distributions of angular momentum, up to $\sim 10^{17} \text{cm}^2 \text{s}^{-1}$, and the uniform vertical magnetic field, we investigate the formation of an accretion disk around a black hole and the jet production near the hole. After material reaches to the black hole with the high angular momentum, the disk is formed inside a surface of weak shock. The disk becomes in a quasi-steady state for stars whose magnetic field is less than 10^{10} G before the collapse. We find that the jet can be driven by the magnetic fields even if the central core does not rotate as rapidly as previously assumed and outer layers of the star has sufficiently high angular momentum. The magnetic fields are chiefly amplified inside the disk due to the compression and the wrapping of the field. The fields inside the disk propagate to the polar region along the inner boundary near the black hole through the Alfvén wave, and eventually drive the jet. The quasi-steady disk is not an advection-dominated disk but a neutrino cooling-dominated one. Mass accretion rates in the disks are greater than $0.01 M_{\odot} \text{s}^{-1}$

¹Department of Electronic Control, Kumamoto National College of Technology, Kumamoto 861-1102, Japan; fujimoto@ec.knct.ac.jp

²*Science & Engineering, Waseda University, 3-4-1 Okubo, Shinjuku, Tokyo 169-8555, Japan*

³*Advanced Research Institute for Science & Engineering, Waseda University, 3-4-1 Okubo, Shinjuku, Tokyo 169-8555, Japan*

⁴ Department of Physics, School of Sciences, Kyushu University, Fukuoka 810-8560, Japan

⁵ Department of Physics, School of Science, the University of Tokyo, 7-3-1 Hongo, Bunkyo-ku, Tokyo 113-0033, Japan

⁶ Research Center for the Early Universe, School of Science, the University of Tokyo, 7-3-1 Hongo, Bunkyo-ku, Tokyo 113-0033, Japan

with large fluctuations. The disk is transparent for neutrinos. The dense part of the disk, which locates near the hole, emits neutrino efficiently at a constant rate of $< 8 \times 10^{51} \text{ergs s}^{-1}$. The neutrino luminosity is much smaller than those from supernovae after the neutrino burst.

Subject headings: Accretion, accretion disks — stars: supernovae: general — MHD — methods: numerical — gamma rays: bursts

1. Introduction

During the collapse of a massive star greater than $35\text{-}40 M_{\odot}$, stellar core is considered to promptly collapse to a black hole (Woosley & Weaver 1995; Heger et al. 2003). Stellar material greater than several solar masses may fall onto the hole at extremely high accretion rates ($> 1 M_{\odot} \text{s}^{-1}$) (Woosley & Weaver 1995; Heger et al. 2003). If the star has sufficiently high angular momentum before the collapse, an accretion disk is likely to be formed around the hole (MacFadyen & Woosley 1999). Jets are suggested to be launched from the inner region of the accretion disk near the hole through magnetic and/or neutrino processes. Gamma-ray bursts (GRBs) are expected to be driven by the jets. This scenario of GRBs is called a collapsar model (Woosley 1993). Assisted by the accumulating observations implying the association between GRBs and the death of massive stars (e.g. Galama et al. (1998); Hjorth et al. (2003); Zeh, Klose, & Hartmann (2004)), the collapsar model seems most promising.

In the light of the collapsar scenario, MacFadyen & Woosley (1999) and MacFadyen, Woosley & Heger (2001) have performed two-dimensional hydrodynamic simulations of rotating massive stars during collapse after the formation of a black hole. Taking account of the viscous heating with α -prescription (Shakura & Sunyaev 1973) and the neutrino cooling, they showed that an accretion disk is formed around the hole if the progenitor has a sufficient range of angular momentum. The disk cools via advection chiefly and the structure of the disk is shown to be well described with a steady, one-dimensional model of an advection dominated accretion flow (ADAF) (Popham, Woosley & Fryer 1999). However, jets cannot be produced in their hydrodynamic simulations. They suggested that collimated outflows can produce through magnetohydrodynamic (MHD) and/or neutrino processes (MacFadyen & Woosley 1999; MacFadyen, Woosley & Heger 2001). Jet propagation through stellar envelope has been investigated via hydrodynamic simulations (Aloy et al. 2000, 2003; Zhang et al. 2003). The jets are shown to be ultrarelativistic and collimated in the envelope, though the jets are assumed to be initiated from the central region of the collapsing star and the thermal energy is deposited at a rate about $10^{51} \text{ergs s}^{-1}$ at the region.

In order to investigate jet production in a collapsar, Proga et al. (2003) have performed MHD simulation of stellar collapse of a rapidly rotating $25M_{\odot}$ progenitor, whose iron core is assumed to a $1.7M_{\odot}$ black hole and magnetic field to be radial (monopole-like) and uniform. They considered neutrino cooling processes in an optically thin regime and resistive heating, whose properties are highly uncertain. In their relatively short (≤ 0.28 s) simulation of a part of the collapsar (about 10km - 5000km), relativistic jets up to $0.2c$ are revealed to be launched and collimated magnetically. Mizuno et.al (2004a) also have shown that relativistic jets ($\leq 0.3c$) are formed in general relativistic MHD calculations of a collapsing massive star of $15M_{\odot}$. Faster jets can be produced near a black hole with larger rotational parameters (Mizuno et.al 2004b). It should be emphasized that their simulations are performed with very small computational domain of $360\text{km} \times 360\text{km}$ and for very short duration about 5ms for a $3M_{\odot}$ black hole. We note that MHD calculation have been performed for a collapsing star with relatively small mass in the previous studies (Proga et al. 2003; Mizuno et.al 2004a,b), though the formation of a black hole is assumed.

On the other hand, jet production via neutrino annihilation is examined with a one-dimensional disc model (Popham, Woosley & Fryer 1999). MacFadyen & Woosley (1999) have estimated the energy deposition rate due to neutrino annihilation to be $\sim 5 \times 10^{50}$ ergs s^{-1} using the disc model (Popham, Woosley & Fryer 1999) and the mass accretion rates obtained from their hydrodynamic simulations. However, the deposition rate highly depends on the structure of the disks. Disks related to GRBs cannot be ADAFs as in MacFadyen & Woosley (1999); Popham, Woosley & Fryer (1999); Proga et al. (2003), but they are a neutrino-cooling dominated flow (NDAF) if neutrino-cooling is more efficient than advective cooling (Narayan, Piran, & Kumar 2001). Properties of NDAF are extensively investigated using one-dimensional, height integrated disk models with detailed micro physics (Kohri & Mineshige 2002; Yokosawa, Uematsu, & Abe 2004) and two-dimensional simulations (Lee & Ramirez-Ruiz 2005). The disks could be convection-dominated flows (Narayan, Piran, & Kumar 2001). Which type of an accretion disk is realized in GRBs could depend on the size of the disk and mass accretion rates through the outer boundary of the disk (Narayan, Piran, & Kumar 2001).

In the present paper, we perform Newtonian MHD simulations of a collapsing massive star of $40M_{\odot}$ to investigate the formation of an accretion disk and the production of jets from the disk in a collapsar. We consider magnetized stars with both rapidly and slowly rotating cores, which are assumed to collapse to a black hole promptly. Our simulations covers from iron core to an oxygen-rich layer of the collapsing star, or 50km-10 000km, and are performed for a long term up to ~ 4 s, which is much longer than the previous studies (Proga et al. 2003; Mizuno et.al 2004a,b), to examine long term evolution of the collapsing star, in particular, properties of the disk and jets during the late phase of the collapse. GRBs related to the final

stage of a massive star have long duration > 2 s. Therefore such long calculation is important for understanding the relation between long GRBs and the disk/jet system formed in the collapsing star.

In §2 we present basic equations of MHD calculation of the collapsing star, a numerical code, and initial conditions of the star. Model parameters and numerical results are shown in §3. We discuss our numerical grid to check resolving magneto-rotational instability (MRI) and compare our results with those obtained in previous works (Proga et al. 2003; Mizuno et.al 2004a) in §4. Finally, we summarize our results in §5.

2. Numerical method and Initial conditions

We carry out Newtonian MHD calculation of the collapse of a rotating massive star of $40M_{\odot}$. In the present study, the core of the star is assumed to be collapsed to a black hole promptly, although the prompt formation of the black hole depends on not only the progenitor mass (or the core mass) but also an equation of state (EOS) and the angular velocity distribution inside the core (e.g. Sekiguchi & Shibata 2004, 2005). Calculation is performed over the region from 50km to 10 000km of the star. Fluid is freely absorbed through the inner boundary of 50km, which mimics a surface of the black hole. The black hole mass, M , is initially set to be that of the central region of the progenitor ≤ 50 km ($0.001M_{\odot}$) and is continuously increased by the mass of the infalling gas through the inner boundary at r_{in} ,

$$\Delta M = \Delta t 4\pi r_{\text{in}}^2 \int_0^{\pi/2} \rho v_r \sin \theta d\theta, \quad (1)$$

during time step Δt , where ρ and v_r are the density and radial velocity estimated at the inner boundary, respectively.

General relativistic hydrodynamic simulations show that black holes are formed at 0.1-0.2 s after the onset of collapse (Sekiguchi & Shibata 2005). In our models, the core is absorbed through the inner boundary and the black hole mass reaches about $2 M_{\odot}$ at the freefall time, $\sqrt{3\pi/32G\rho_c} \sim 0.1$ s, after the onset of the collapse, as we shall see later. Here ρ_c is the core density of $\sim 10^{10} \text{g cm}^{-3}$. Hence, our procedure can approximate the collapsing phase to a black hole in an appropriate level. We note that Proga et al. (2003) have performed an MHD simulation after the formation of a black hole of $1.7M_{\odot}$.

2.1. Input Physics and Numerical Code

To calculate the structure and evolution of the collapsing star, we solve the Newtonian MHD equations,

$$\frac{D\rho}{Dt} + \rho \nabla \cdot \mathbf{v} = 0, \quad (2)$$

$$\rho \frac{D\mathbf{v}}{Dt} = -\nabla P - \rho \nabla(\Phi + \Psi) + \frac{1}{4\pi} (\nabla \times \mathbf{B}) \times \mathbf{B}, \quad (3)$$

$$\rho \frac{D}{Dt} \left(\frac{e}{\rho} \right) = -P \nabla \cdot \mathbf{v} - L_\nu, \quad (4)$$

$$\frac{\partial \mathbf{B}}{\partial t} = \nabla \times (\mathbf{v} \times \mathbf{B}), \quad (5)$$

$$\Delta \Phi = 4\pi G \rho, \quad (6)$$

where $\rho, \mathbf{v}, P, \Phi, \Psi, \mathbf{B}, e$, and L_ν are the mass density, the fluid velocity, the pressure other than the magnetic pressure, the gravitational potential of fluid, the gravitational potential of the central object, the magnetic field, the internal energy density, and the neutrino cooling rate, respectively. We denote the Lagrange derivative as D/Dt .

The numerical code for the MHD calculation employed in this paper is based on the ZEUS-2D code (Stone & Norman 1992). We have extended the code to include a realistic EOS (Kotake et al. 2004) based on the relativistic mean field theory (Shen et al. 1998). For lower density regime ($\rho < 10^5 \text{ g cm}^{-3}$), where no data is available in the EOS table with the Shen EOS, we use another EOS, which includes contributions from an ideal gas of nuclei, radiation, and electrons and positrons with arbitrary degrees of degeneracy (Blinnikov et al. 1996). We carefully connect two EOS at $\rho = 10^5 \text{ g cm}^{-3}$ for physical quantities to vary continuous in density at a given temperature.

We consider neutrino cooling through electron-positron pair capture on nuclei, electron-positron pair annihilation, and nucleon-nucleon bremsstrahlung. The total neutrino cooling rate is evaluated with a simplified neutrino transfer model based on the two-stream approximation (Di Matteo, Perna, & Narayan 2002), with which we can treat the optically thin and thick regimes on neutrino reaction approximately. We ignore resistive heating, whose properties are highly uncertain, not as in Proga et al. (2003). We note that the change in the electron fraction, Y_e , is ignored in the MHD calculation (or, $DY_e/Dt = 0$).

Spherical coordinates, (r, θ, ϕ) are used in our simulations and the computational domain is extended over $50 \text{ km} \leq r \leq 10000 \text{ km}$ and $0 \leq \theta \leq \pi/2$ and covered with $200(r) \times 24(\theta)$ meshes, with which we can resolve a fastest growing mode of MRI for most models (see details in §4.1). The location of the inner boundary is greater than that in Proga et al.

(2003) (~ 10 km). We discuss how the location of the inner boundary affects our numerical results later (§4.2). We fix ratios of the size of the meshes as $\Delta r_{k+1}/\Delta r_k = 1.02$ ($\Delta r \geq 1 \times 10^6$ cm) and $\Delta \theta_{k+1}/\Delta \theta_k = 1$. We assume the fluid is axisymmetric and the mirror symmetry on the equatorial plane. We mimic strong gravity around the black hole in terms of the pseudo-Newtonian potential (Paczynski & Wiita 1980):

$$\Psi = -\frac{GM}{r - r_g}, \quad (7)$$

where G is the gravitational constant and $r_g = 2GM/c^2$ is the Schwarzschild radius.

2.2. Initial conditions

We set the initial profiles of the density, temperature, internal energy density, and electron fraction to those of the spherical model of a $40M_\odot$ massive star before the collapse (Hashimoto 1995). The radial and azimuthal velocities are set to be zero initially, and increase due to the collapse induced by the central hole and self-gravity of the star. The computational domain is extended from the iron core to an inner oxygen layer. The star of about $4M_\odot$ is enclosed with the computational domain. The boundaries of the silicon layers between the iron core and the oxygen layers are located at about 1800 km ($1.88M_\odot$) and 3900km ($2.4M_\odot$), respectively. We adopt an analytical form of the angular velocity $\Omega(r)$ of the star before the collapse:

$$\Omega(r) = \Omega_0 \frac{R_0^2}{r^2 + R_0^2}, \quad (8)$$

as in the previous study of collapsars (Mizuno et.al 2004a,b) and SNe (Kotake et al. 2004; Yamada & Sawai 2004). Here Ω_0 and R_0 are parameters of our model. We consider two sets of (Ω_0, R_0) ; (10 rad s⁻¹, 1000km) (case with rapidly rotating core) and (0.5 rad s⁻¹, 5000km) (case with slowly rotating core). For these sets of Ω_0 and R_0 , the maximum specific angular momentum is about 10^{17} cm² s⁻¹, which is comparable to that of the Keplerian motion around a black hole of $3M_\odot$ at 50km. Therefore the centrifugal force can be larger than the gravitational force of the central black hole and the formation of a disk-like structure is expected near the hole. Figure 1 shows the specific angular momentum distribution on the equatorial plane for two cases and for the previous works (MacFadyen & Woosley 1999; Proga et al. 2003). The angular momentum for the two cases are comparable near the outer boundary of the computational domain. We find that the specific angular momentum adopted in MacFadyen & Woosley (1999) is similar to those for the model with $\Omega_0 = 10$ rad s⁻¹ and $R_0 = 1000$ km.

Initial magnetic field is assumed to be uniform, parallel to the rotational axis, and

weak elsewhere ($\beta = 8\pi P/B^2 \gg 1$). We consider cases with the initial magnetic field, $B_0 = 10^8, 10^{10}$ and 10^{12} G. It should be noted that the magnetic pressure is much smaller than the other pressure even if B_0 is equal to 10^{12} G. The models are labeled by R8, R10, R12, S8, S10, and S12, in which the first character, R(rapidly rotating core) or S(slowly rotating core), indicates the set of Ω_0 and R_0 , and the numeral, 8, 10, and 12, equals $\log_{10}(B_0/\text{G})$.

3. Numerical Results

We summarize model parameters and features in Table 1. Columns (2) through (4) give model parameters, with which initial conditions are represented for each model. Column (5) gives the time at the end of each run, $t = t_f$, after the onset of collapse, at which t is equal to 0. Column (10) gives the the mass of the black hole at $t = t_f$. Simulations for models with $B_0 = 10^8, 10^{10}$, and, 10^{12} G are performed for $3 \times 10^5, 2 \times 10^5$, and 1×10^5 time steps, respectively. Columns (6) and (7) ((8) and (9)) give ratios of the rotational (magnetic) to the potential energy integrated over the computational domain at $t = 0$ and $t = t_f$, respectively.

As we shall see later, jets are produced near the black hole for R10, R12, S10, and S12. Properties of the jets are summarized in Table 2. Column (2) gives t_{jet} when jets are passed through 1000km. Columns (3), (4), (5), and (6) represent the mass, magnetic, kinetic, and internal energies of the jets, respectively. The mass and energies of the jets are defined as those ejected through the outer boundary.

3.1. Collapse of a star with a rapidly rotating core

3.1.1. MHD features

We present magnetohydrodynamic features of the collapsing star for R10 as a representative case. Figure 2 shows contours of density (left panels) and those of the ratio of P_{mag} to the pressure (right panels) for R10 at $t = 1.6625, 2.0193$, and, 2.6225 s. Initially, the star collapses nearly spherical and becomes aspherical gradually as the gas accretes with higher angular momentum. When the gas with $\sim 10^{17} \text{cm}^2 \text{s}^{-1}$ falls the black hole (~ 0.1 s), weak shock appears near the remnant and propagates outward slowly (top and middle left panels). The propagation velocity of the shock is several thousands km s^{-1} , which is much larger than the Alfvén velocity and slightly less than the sound velocity. A disk-like structure forms inside the shock (top left panel). We find that after the formation of the disk, the flow consists of the three parts; (i) the nearly spherical inflow outside the shock, (ii) the quasi-steady, equilibrium disk, and (iii) the inflow along the disk surface. The disk is in

quasi-steady state and supported by the centrifugal force mainly and the gas pressure, which is larger than the magnetic pressure. The magnetic pressure is enhanced inside the disk (top and middle right panels) and finally drives a jet, whose expansion velocity reaches $0.1c$ near the black hole along the rotational axis as we can see later (Figure 3). In this region the density drops below 10^7g cm^{-3} (bottom left panel), the radial and toroidal components of the magnetic field are 10^{14}G , and the magnetic pressure is greater than the gas pressure (bottom left panel).

We pay attention to a region near the inner boundary ($300\text{km} \times 300\text{km}$) to investigate the generation of jets. We can clearly see the phase of jet production in Figure 3, in which contours of P_{mag} for R10 at $t = 2.5301, 2.5340$, and, 2.5368s (from left to right) are presented. The magnetic fields are amplified inside the disk and propagates just above the inner boundary to the polar region via the Alfvén wave (left and center panels). The wave is enough fast ($\sim 10\,000 \text{ km s}^{-1}$) to propagate along the boundary before the infall to the black hole along with the accreting gas. The jets are eventually driven by the magnetic pressure near the boundary (center panel) and ejected along the rotational axis (right panel). In this way, the magnetic energy, which is enhanced inside the disk, can be transported to the jets.

We calculate another model with the same angular velocity distribution as R10 but without magnetic field, or R0, to examine the cause of the weak shock. We find that a weak shock also appears in this non-magnetized model. Therefore, the shock seems not to be originated from any magnetic processes. It is possibly generated via centrifugal barrier. We also note that similar accretion shock have appeared in a hydrodynamic simulation of a collapsar (MacFadyen & Woosley 1999).

It is pointed out that the magnetic field is exponentially amplified through MRI in an accretion disk (Balbus & Hawley 1998). Similar amplification of the magnetic field is also suggested to occur in a rotating star during collapse from one-dimensional calculations (Wheeler, Meier, & Wilson 2002; Akiyama et.al 2003). We examine the field amplification in our two-dimensional models of a rotating massive star. Figure 4 shows the time evolution of the magnetic fields integrated over the computational domain. We denote $\int (B_i^2/8\pi)dV$ as $E_{m,i}$ ($i = r, \theta, \phi$). The initial magnetic field is vertical so that the toroidal component of the magnetic field vanishes and $E_{m,r} = E_{m,\theta}$ initially. After the accretion of high angular momentum material ($t \geq 0.1 \text{s}$), the radial and azimuthal components of the magnetic field are amplified exponentially in time and the toroidal component is rapidly enhanced. We note that the MRI of the vertical magnetic field produces the X component of the magnetic field and the wrapping of the poloidal field generates the toroidal field. We find that the amplification of the radial and azimuthal fields is mainly due to compression of the field initially and MRI in the later phase and that the toroidal field can be amplified by wrapping of the seed poloidal

field. In fact, the radial and azimuthal fields are amplified as $\exp(t/0.1 \text{ s})$, as shown in Figure 4, and the growth timescale of MRI, τ_{MRI} , is $\sim 0.1 \text{ s}$. On the other hands, the characteristic timescale for the field wrapping, τ_{WRAP} , is calculated as

$$\begin{aligned}\tau_{\text{WRAP}} &= 4\pi \left| \frac{\frac{\partial B_\phi}{\partial t}}{B_\phi} \right|^{-1} \\ &= 4\pi \left| \frac{B_X}{B_\phi} \left(X \frac{\partial \Omega}{\partial X} \right) + \frac{B_Z}{B_\phi} \left(X \frac{\partial \Omega}{\partial Z} \right) \right|^{-1}\end{aligned}\quad (9)$$

(Takiwaki et al. 2004). Here B_X and B_Z are the X and Z -components of the magnetic field, respectively. The toroidal magnetic field is therefore rapidly enhanced through the field wrapping if the poloidal field dominates over the toroidal one and the gas is differentially rotating. This is the case in R10 at $t \sim 0.1 \text{ s}$. We note that τ_{WRAP} is shorter than τ_{MRI} during the rapid amplification phase of the toroidal field ($t \sim 0.1 \text{ s}$) as in a magnetized core collapse SN (Takiwaki et al. 2004). As the toroidal field increases, τ_{WRAP} becomes longer (eq. (9)). After the toroidal field becomes comparable to the poloidal field ($t > 0.1 \text{ s}$), the growth timescale of the toroidal magnetic field is comparable to that of the poloidal field. Note that τ_{MRI} ($\sim 0.1 \text{ s}$) becomes comparable or shorter than τ_{wrap} in this phase. Because our two-dimensional axisymmetric simulations cannot follow the amplification of the toroidal magnetic field due to MRI, the toroidal field may be saturated as a lower level. At the end of the simulation, the total magnetic energy, kinetic, and rotational energies are 0.57×10^{51} , 1.52×10^{51} , and 1.50×10^{51} ergs, respectively.

For higher initial magnetic field of the progenitor, the magnetic field is more rapidly amplified than R10. Figure 5 shows contours of density (left panels) and those of the ratio of P_{mag} to the pressure (right panels) for R12 at $t = 0.2378$ and 0.3560 s . A jet launches by the magnetic pressure (right top panel) just after the formation of a disk (left top panel) near the central remnant along the rotational axis. In the polar region, the radial and toroidal components of the magnetic field are comparable and reach 10^{15} G just before the launch of the jet. It should be emphasized that the density of the jet in R12 is much higher than that of R10. Figure 11 shows various time scale in jets. Solid, dashed, and, dotted lines denote the ejection time, the neutrino cooling time through pair capture, and, that via pair annihilation, respectively. We find that the ejection time is much smaller than the neutrino cooling time and that jets cannot be cooled through neutrino.

For lower initial magnetic field, hydrodynamic features are similar to R10. For R8, a disk-like structure is formed inside a shock surface as in R10. The disk is in quasi-steady state and is supported by the centrifugal force and the pressure gradient. The radial velocity is lower than the rotational velocity, which has a Keplerian profile, by about three orders of

magnitude. The magnetic pressure is lower than the gas pressure elsewhere, and the toroidal component of the field attains to 10^{14} G.

3.1.2. Disk properties

To examine properties of the disk, we present physical quantities near the equatorial plane ($\theta = 88.1^\circ$) in Figure 6, for R10 at 1.6625 s, at which the weak shock propagates near 2000km (top left panel in Figure 2). The radial velocity is lower than the near-Keplerian rotational velocity by about two orders of magnitude. The disk is in equilibrium and mainly supported by the centrifugal force, which is greater than the pressure gradient near the black hole. Inside the shock surface, the flow is highly convective (bottom left panel), which is clearly seen in Figure 7. Here contours of the ratio of P_{mag} to the pressure are shown at an inner region (500km \times 500km) for R10 at $t = 1.6625$ s (top right panel in Figure 2). We find that inside the disk, velocity field is highly complicated so that the magnetic field has also rather complex structure.

Figure 8 shows contour of logarithmic specific neutrino cooling rate through pair capture on nuclei, for R10 at 1.6625 s, defined as

$$q_{\text{cap}} = 9.2 \times 10^{23} \rho X_{\text{nuc}} \left(\frac{T}{10^{11} \text{K}} \right)^6 \text{ ergs s}^{-1} \text{ cm}^{-3}, \quad (10)$$

where X_{nuc} is the mass fraction of nucleons and is approximated with

$$X_{\text{nuc}} = 8.2 \times 10^8 \frac{T_{\text{MeV}}^{9/8}}{\rho^{3/4}} \exp(-7.074/T_{\text{MeV}}), \quad (11)$$

or unity, whichever is smaller with the temperature in MeV, T_{MeV} (Woosley & Baron 1992). Density contours of $10^8, 10^9, 10^{10}$, and 10^{11} g cm $^{-3}$ are plotted on Figure 8. We find that neutrino cooling is efficient inside the shock, where the temperature is higher than 10^{10} K via shock heating, and much efficient near the equatorial plane of the disk with high densities because of more efficient pair capture in denser regions. Neutrino luminosity stays at a constant level about 5×10^{51} ergs s $^{-1}$, as we shall see later (Figure 17). We find that neutrino cooling via e^\pm capture dominates over those through electron-positron pair annihilation and nucleon-nucleon bremsstrahlung by one or two orders of magnitude inside the disk (bottom panels in Figure 9).

At an inner region of disks, neutrino cooling time via e^\pm capture, e/q_{cap} , which is 0.1-1 s, is comparable or smaller than accretion time, $|r/v_r|$ (bottom panels in Figure 9). Thus, the disks cool not advection but neutrino emission in the region. Indeed, we find that the

density and temperature profiles are well described with those of *not ADAF but NDAF*, or, $\rho \sim r^{-51/20}$ and $T \sim r^{-3/10}$ (top panels in Figure 9). For ADAF, the profiles have different power laws, or, $\rho \sim r^{-3/2}$ and $T \sim r^{-5/8}$ (e.g., Fujimoto et al. 2000). We note that the gas pressure is dominated over the radiation and degenerate pressure in our models other than outer part of the disks, where the radiation pressure is comparable to the gas pressure (bottom right panel in Figure 6). The magnetic pressure is lower than the pressure other than the region near the rotational axis where the toroidal component of the field is amplified to 10^{15} G (top right panel in Figure 6).

In order to examine whether the disk is opaque to neutrino or not, we calculate the height h_ν at which the neutrino optical depth $\tau_\nu(R)$ is equal to $2/3$,

$$\tau_\nu(R) = \int_{h_\nu(R)}^{h_{\max}(R)} \rho(R, z) \kappa_\nu(R, z) dz = \frac{2}{3}, \quad (12)$$

as in Surman & McLaughlin (2003). Here h_{\max} and κ_ν are the height of the computational domain from the equatorial plane and the neutrino opacity at the distance from the rotational axis, R . We note that the optical depth is simply set to be the sum of the depths for e , μ , and τ neutrinos. The neutrino decoupling surface is found to be torus-like and very limited to the inner region ($\leq 100\text{km}$) of the disk near the black hole if exists. For $t \geq 0.3\text{s}$, the surface is located at the region below 30km from the equatorial plane near the hole. We find that almost disk is therefore optically thin to neutrino, and that neutrino is hardly trapped inside the disk.

Figure 10 shows the time evolution of the accretion rate through the inner boundary at 50km , defined as,

$$\dot{M} = 4\pi r^2 \int_0^{\pi/2} \rho v_r \sin \theta d\theta, \quad (13)$$

where ρ and v_r are estimated at the boundary. The rates through parts of the boundary, \dot{M}_{pol} ($\theta \leq 20^\circ$) and \dot{M}_{disk} ($\theta \geq 50^\circ$), are also presented in Figure 10. At the beginning of the collapse, material with low angular momentum falls through the inner boundary at very high accretion rates ($\geq 10M_\odot \text{s}^{-1}$) for the freefall time of core ($\sim 0.1\text{s}$). As gas accretes onto the black hole with high angular momentum ($t \geq 0.1\text{s}$), the polar infall dominates over the disk accretion. \dot{M}_{disk} is much lower than \dot{M} , which is comparable with \dot{M}_{pol} , by one order of magnitude. During quasi steady collapse ($t > 1.0\text{s}$), \dot{M} is $\sim 0.2\text{--}0.5 M_\odot \text{s}^{-1}$ with fast fluctuations and gradual decrease. \dot{M}_{disk} varies between $0.02M_\odot \text{s}^{-1}$ and $0.07M_\odot \text{s}^{-1}$ in this phase and sharply decreases after the ejection of the jet.

3.2. Collapse of a star with a slowly rotating core

Now we move on to models with slowly rotating core, or S8, S10, and S12. As we can see in Figure 1, the initial angular momentum for these models is smaller than $10^{17} \text{cm}^2 \text{s}^{-1}$ except in the outer part of the computational domain. Most of the inner region of the star therefore collapse to a black hole. Material with high angular momentum is expected to form a disk-like structure. Figure 12 shows contours of density (left panels) and those of the ratio of P_{mag} to the pressure (right panels) for S10 at $t = 1.0207$ and 1.3134 s. The core for S10 rotates slower than that for R10. The star collapses with nearly spherical configuration for a longer time. When the rapidly rotating gas falls near the black hole ($t \sim 0.45$ s), the magnetic field has been amplified due to field compression and wrapping initially and MRI later. Eventually, a magnetically driven jet is found to be generated from a central region near the black hole (bottom panels in Figure 12), although the core rotates slowly. We find that the jet is less collimated than that in R10 (bottom left panels in Figures 2 and 12).

A disk like structure is formed as in R10 but magnetically driven winds arise near the equatorial plane (top left panel in Figure 12), which disappear in R10. Figure 13 shows physical quantities near the equatorial plane ($\theta = 88.1^\circ$) for S10 at $t = 0.5676$ s. When gas infall to the remnant with high angular momentum, the magnetic field has been amplified so large that the magnetic pressure is comparable to the gas pressure near the central remnant. Consequently, the winds are driven via magnetic and gas pressure for S10, in contrast to R10. These magnetically driven winds have high velocity ($\sim 0.1c$; bottom left panel in Figure 13) and relatively high entropy of $s \sim 20$ (top left panel in Figure 13) where s is the entropy per baryon in units of the Boltzmann constant. Distributions of the density, temperature and pressure cannot be described with those of simple power laws in r , in contrast to R10, due to the winds.

As in cases with rapidly rotating core, the toroidal magnetic field is more rapidly amplified in models with a larger initial magnetic field. We find that S12 also launches a jet from a central region near the black hole along the rotational axis. Figure 14 shows contours of density (left panel) and those of the ratio of P_{mag} to the pressure (right panel) for S12 at $t = 0.2812$ s. The jet is collimated in a wider region compared with that in R12 (bottom panels in Figure 14) because of slow core rotation in S12. It is noted that the jet has density lower than that in R12.

For S8, as in R8 and R10, a disk-like structure is formed inside a shock surface located at 800km on the equator at the end of the computation, and the disk is well described with a quasi-steady NDAF rotating with a Keplerian profile. The magnetic pressure, whose toroidal component attains to 10^{15} G, is lower than the gas pressure elsewhere. Magneto-centrifugal winds are not appeared in S8, in contrast to S10, and jet cannot be produced in S8, as in

R8.

In brief, the collapsing star can originate well collimated jets if the star has sufficiently large magnetic field and rapidly rotating core. On the other hands, when the star has not rapidly rotating core but envelope with sufficiently high angular momentum, the star can drive less collimated jets. The jet could be generated from collapsing stars with non-rotating core and sufficiently high angular momentum envelope and large magnetic field.

3.3. Time Evolution of Collapsing Star

We present the time evolution of various quantities, such as the magnetic energy, the mass accretion rate, and the neutrino luminosity of our models to compare properties of models each other.

Figure 15 shows the time evolution of the magnetic energy integrated over the computational domain, $E_m = \int (B^2/8\pi)dV$, for all models. We note that the toroidal field dominates over the other components of the field, as in R10 (Figure 4). The fields are amplified earlier as the initial magnetic field increases and the core rotation becomes faster. This is because the magnetic field is mainly amplified by the wrapping of the field. Rapid differential rotation is therefore required from the amplification.

Figure 16 shows the time evolution of \dot{M} for rapidly rotating models, or R models (upper panel) and slowly rotating models, or S models (bottom panel). At the beginning of the simulations ($t < 0.1$ s), \dot{M} roughly are comparable for all models because the collapse is almost spherical and effects of rotation and magnetic field can be neglected in this phase. After the infall of higher angular momentum material, \dot{M} rapidly drops due to the centrifugal barrier. This is because \dot{M} in R models are smaller than those of S models during an initial phase ($t \leq 0.5$ s). Once a disk-like structure is formed (for R8, R10, S8, and S10), \dot{M} stays 0.2-0.3 $M_\odot \text{ s}^{-1}$ with fast fluctuations. We note that \dot{M}_{disk} is much lower than \dot{M} by about an order of magnitude for all models, as in R10 (Figure 10).

Figure 17 shows the time evolution of the neutrino flux integrated over the computational domain, or the neutrino luminosity, L_ν , for all models. Neutrino is initially emitted from a quasi-spherically collapsing dense core near the black hole at the maximum rate of $\sim 10^{52} \text{ ergs s}^{-1}$ around ~ 0.1 s. For R8 and R10, material with high angular momentum reaches to the hole before the infall of the entire dense core to the hole. Neutrino continues to be emitted from a disk formed near the equator (Figure 8 for R10) so that L_ν stays roughly constant at the rate of $5\text{-}6 \times 10^{51} \text{ ergs s}^{-1}$. Note that the neutrino luminosity is much smaller than that for SN $\sim 5\text{-}6 \times 10^{52} \text{ ergs s}^{-1}$ at 0.1 s after core bounce (Liebendörfer et al. 2001)

because in SN, neutrino is efficiently emitted from a region near a proto neutron star. We note that the neutrino luminosity slightly increases if we adopt much smaller inner boundary, as we shall see later (§4.2). On the other hand, for S8 and S10, high angular momentum material falls to the hole after the accretion of the entire dense core. L_ν therefore drops sharply around 0.1 s and raises rapidly when a rotationally supported disk is formed near the equator ($t \sim 1.0$ s and 0.6 s for S8 and S10, respectively).

4. Discussion

4.1. Numerical resolution of our simulations

If the fastest growing mode of MRI is unresolved, saturation of the MRI occurs later and at a lower amplitude of the magnetic energy (Stone & Pringle 2001). Hence, we check whether our numerical grid can resolve the fastest growing mode of MRI, whose wavelength is given by $\lambda_c = 2\pi v_A / \sqrt{3}\Omega$ where v_A is the Alfvén velocity. We need to verify the relation, $\Delta r < \lambda_c$, which leads to

$$\frac{\Delta r}{r} < \frac{2\pi v_A}{\sqrt{3}v_\phi}, \quad (14)$$

where Δr is the grid size. At the beginning of simulations, the relation (14) cannot hold because of small v_A compared with v_ϕ . However, the core is stable against MRI in this phase because Ω is nearly constant (see the initial distribution (eq. 8)).

After the formation of a disk-like structure, the disk becomes to be unstable to MRI. The growth time scale of MRI, τ_{MRI} , is comparable to that of the wrapping of the field τ_{wrap} (~ 0.1 s). However, the relation (14) cannot hold. The magnetic field is therefore amplified by the field wrapping mainly. As the field increases, v_A becomes greater. We find that the relation (14) holds at a later time (~ 0.2 s for R10) and our numerical grid can resolve, albeit marginally, the fastest growing mode of MRI, by which the field is amplified to a saturated value. For R8, however, the relation (14) cannot hold so that the magnetic energy is possibly saturated at a lower amplitude. We need finer numerical grids to resolve MRI for R8.

4.2. The location of the inner boundary and the numerical grids

In the present study, the inner boundary of the computational domain is set to be 50 km, which is larger than that in Proga et al. (2003) (~ 10 km). In order to examine the dependence of disk properties on the location of the inner boundary, r_{in} , we have performed a MHD simulation of R10 with a smaller inner boundary of 10 km and with finer 220 radial

meshes until $t \sim 0.8$ s.

Figure 18 shows radial profiles of the density (solid lines) and temperature (dotted lines) near the equatorial plane ($\theta = 88.1^\circ$) in R10 at 0.5 s for $r_{\text{in}} = 10\text{km}$ and 50km . Thick and thin lines correspond to the profiles for $r_{\text{in}} = 10\text{km}$ and 50km , respectively. We also plot profiles of the density (dotted line) and temperature (dot-dashed lines) of NDAF, as shown in Figure 9. We find that the profiles are independent of the location of the inner boundary. Radial profiles of other physical quantities inside the disk are also independent of the location. We also find that the disk is neutrino-cooling dominated even if we adopt the smaller inner boundary of 10km . The neutrino luminosity slightly increases to $1.20 \times 10^{52}\text{ergs s}^{-1}$ from $0.81 \times 10^{52}\text{ergs s}^{-1}$ for $r_{\text{in}} = 50\text{km}$. The luminosity has a trend of gradual decrease after the formation of the disk-like structure for $r_{\text{in}} = 50\text{km}$ (Figure 17). For $r_{\text{in}} = 10\text{km}$, the luminosity decreases to $< 1 \times 10^{52}\text{ergs s}^{-1}$ after $t = 0.55\text{ s}$ and stays roughly constant at the rate of $7\text{--}8 \times 10^{51}\text{ergs s}^{-1}$ for $t = 0.6\text{--}0.8$ s. Furthermore, the disk is found to be optically thin to neutrino for $t > 0.5\text{ s}$, as in case with $r_{\text{in}} = 50\text{km}$.

We impose the mirror symmetry on the equatorial plane, which is not assumed in Proga et al. (2003). If we calculate without the symmetry, the convective motion near the equatorial plane may be weakened and jets may become less collimated. We need calculation in a computational domain with $0 \leq \theta \leq \pi$ grids to examine such the possibility. Moreover, in light of the collapsar model, it may be important to investigate standing accretion shock instability that is not appeared in calculation with the mirror symmetry and whose importance has been recognized in SN explosion (Blondin et al. 2003).

4.3. Comparison between Our Models and Previous Works

In MHD simulations of a $25M_\odot$ collapsar (Proga et al. 2003) and a $15M_\odot$ collapsar (Mizuno et.al 2004a,b), a jet has been shown to be produced magnetically near the black hole, as in our results. We compare our results and those obtained by other groups (Proga et al. 2003; Mizuno et.al 2004a,b).

We firstly compare disk properties of our model R10 (Figure 6) and those in Proga et al. (2003) (in their Figure 3). We note however that Figure 6 shows the properties at $t = 1.6625\text{ s}$ while Figure 3 in Proga et al. (2003) shows time-averaged properties during $t = 0.2629\text{--}0.2818$ s. In Proga et al. (2003), the $25M_\odot$ collapsar is simulated with a similar distribution of the angular momentum and the magnetic field as in our models after the formation of a black hole of $1.7M_\odot$, which is the mass of an entire iron core. They assume non-rotating inner Si and O layers and set the initial distributions of velocity and density

to be those of one-dimensional free-fall gas. They have taken into account resistive heating and neutrino cooling in an optically thin regime, and ignored self-gravity of the star.

On the other hands, we have simulated the collapse of a $40 M_{\odot}$ star, whose core is assumed to collapse to a black hole promptly. The initial distributions of physical quantities are set to be those of presupernova and collapse to the black hole is mimicked with the absorption of material through the inner boundary. We have ignored resistive heating but considered neutrino cooling with the two-stream approximation (Di Matteo, Perna, & Narayan 2002), with which we can treat the optically thin and thick regimes on neutrino reaction approximately.

The radial velocity for R10 is much slower than that in Proga et al. (2003) (in their top-right panel of Figure 3). The difference is attributed to the existence of the weak shock, where the radial velocity sharply drops (left bottom panel in Figure 6). The cause of the weak shock is possibly the centrifugal barrier as seen in §3.1.1. Note that a similar accretion shock is also revealed in hydrodynamic calculations of the collapse of a $35 M_{\odot}$ star (MacFadyen & Woosley 1999). Disappearance of the weak shock in Proga et al. (2003) probably inherits their initial distributions of the inner layers above mentioned. We note that the radial velocity inside the disk is much smaller than that in Proga et al. (2003) even if the calculation is performed for $r_{\text{in}} = 10$ km.

The slower radial velocity leads to longer accretion time. Thus, the cooling time via neutrino is shorter than the accretion time in the present study (Figure 9), in contrast with Proga et al. (2003). Hence the disk is neutrino-cooling dominated in our models while advection-dominated in their model except for a small region inside the torus where the density reaches maximum. We note that the disk structure obtained from the MHD calculation in the present study is different from that through hydrodynamic one with α -viscosity (MacFadyen & Woosley 1999), in which the structure is roughly coincident with that of ADAF.

The accretion rate through the inner boundary is estimated to be about $5 \times 10^{32} \text{g s}^{-1}$ ($= 0.25 M_{\odot} \text{s}^{-1}$) with fast fluctuations (Proga et al. 2003), which is comparable with the rates in R8, R10, S8, and S10 after the formation of the quasi-steady disk (see Figure 10). The radial profiles of the magnetic fields are similar as those of Proga et al. (2003) but the magnitudes are higher. The magnetic energy in Proga et al. (2003) is smaller than that in our models up to one order of magnitude at the end of the calculation, in spite of greater initial magnetic energy; $E_{m,r}$ is about $2 \times 10^{47} \text{ergs s}^{-1}$ (in their Figure 1). A jet is magnetically driven from the inner region of the disk in our models and Proga et al. (2003) and the jet velocity is comparable.

Moreover, we compare disk properties of our model R10 for $r_{\text{in}} = 10 \text{km}$ at $t = 0.5 \text{s}$

(Figure 18) and those in Proga et al. (2003) (in their Figure 3). We find that the radial profiles of the density and temperature in our calculation are similar to those in Proga et al. (2003). The density has a maximum of $10^{12} \text{ g cm}^{-3}$ around $\sim 30\text{-}40$ km. The radial velocity rapidly increases near the inner boundary because of strong gravity of the black hole. The density in our run is greater than that in Proga et al. (2003) due to smaller radial velocity, while the temperature is cooler. In Proga et al. (2003), the accretion time is shorter than that in our run due to greater radial velocity. The liberated energy is therefore advected into the black hole with the accreting gas, which cools via neutrino inefficiently and becomes hotter than that in our model. The resistive heating, which is considered in their model and not in our models, could also heat the accreting gas to higher temperature. Consequently, the neutrino luminosity, which is very sensitive to the temperature (eq. (10)), is greater than that in our run.

Next we compare our results with those of scale-free, general relativistic MHD simulations (Mizuno et.al 2004a) for a $3M_{\odot}$ black hole and a density unit of $10^{10} \text{ g cm}^{-3}$. They have simulated the collapse of a magnetized, rotating massive star after the formation of the black hole for very short duration about 5 ms using a simplified (gamma-law) EOS and very small computational domain of $360\text{km} \times 360\text{km}$. Initial profiles of the angular velocity and the magnetic field are similar as in our models, but their model A2 corresponds to $\Omega_0 = 378 \text{ s}^{-1}$ and $B_0 = 1.5 \times 10^{13} \text{ G}$, which is much faster rotation and greater initial field than R12. A magnetically-driven jet is shown to emit near the hole and propagate along the rotational axis with a speed of up to $0.2c$ at 5 ms much earlier than R12 because of faster rotation and greater initial magnetic field.

Our simulations are performed with the Newtonian MHD code, in which the pseudo-Newtonian potential is used to mimic general relativistic effects of a black hole. If we examine during the collapsing phase to the black hole or more inner region near the black hole, we need general relativistic MHD code as in Mizuno et.al (2004a,b) and Sekiguchi & Shibata (2004, 2005). However, our numerical grid covers the region with $r \geq 50$ km, or, $5.56r_g$ of a $3M_{\odot}$ black hole. General relativistic effects are therefore small for our models.

4.4. Implication for GRB progenitors

Taking into account angular momentum transport through magnetic torque, whose importance on evolution of massive stars is shown in Spruit (2002), Heger et al. (2004, 2005) and Maeder & Meynet (2004) have performed 1.5 dimensional simulations on evolution of rotating massive stars. They showed that the iron-core of the stars has specific angular momentum up to $\sim 10^{15} \text{ cm}^2 \text{ s}^{-1}$ before core collapse. It is much smaller than the specific

angular momentum of material with the Keplerian motion around a $2 M_{\odot}$ black hole at the last stable circular orbit, $2 \times 10^{16} \text{cm}^2 \text{s}^{-1}$. Consequently, single massive stars are claimed not to be a progenitor of GRB if the magnetic braking mechanism of Spruit (2002) operates in the stars (Petrovic et al. 2005; Fryer & Heger 2005). Moreover, even in a binary companion star (Petrovic et al. 2005), a rapidly rotating core with the specific angular momentum of $2 \times 10^{16} \text{cm}^2 \text{s}^{-1}$ is unlikely to be realized though such core can be produced in the merger of two helium cores during common-envelope inspiral phase of a binary system (Fryer & Heger 2005). It should be emphasized however that the angular momentum transport through magnetic torque in a massive star is still uncertain.

Moreover, even for stars with a slowly rotating iron core, an accretion disk around a black hole is formed during the collapse of the stars and a jet can be produced from the disk near the hole if outer layers of the stars have a sufficiently high angular momentum, as shown in §3.2. Therefore, progenitors of GRB could not always be required for a rapidly rotating iron core; The progenitors may require to have layers with a sufficiently high angular momentum and a sufficiently high magnetic field.

5. Concluding Remarks

We have performed two-dimensional, axisymmetric MHD simulations of the collapse of a $40 M_{\odot}$, rapidly rotating star, whose core is assumed to collapse to a black hole promptly and angular momentum attains to $10^{17} \text{cm}^2 \text{s}^{-1}$, to examine the formation of an accretion disk around the black hole and the jet production near the hole in the light of the collapsar model of GRB. Considering two distributions of the angular velocity and the uniform magnetic field, whose magnitude is 10^8 , 10^{10} , and 10^{12} G, parallel to the rotational axis, inside the star before collapse, we investigate how angular momentum and magnetic field distributions inside the star affect the jet production and the disk properties. We summarize our conclusions as follows;

1. After material reaches to the black hole with high angular momentum of about $10^{17} \text{cm}^2 \text{s}^{-1}$, a disk is formed inside a surface of weak shock, which is appeared near the hole due to the centrifugal force and propagates outward slowly. The disks become a quasi-steady state for models with the initial magnetic field less than 10^{10} G.
2. We find that the jet can be driven by the tangled-up magnetic fields even if the central core does not rotate as rapidly as previously assumed and outer layers of the star has a sufficiently high angular momentum.
3. The jet is driven by the magnetic field, which is dominated by the toroidal component

and is amplified due to the wrapping of the field, as long as the initial magnetic field is greater than 10^{10}G . The field are chiefly amplified inside the disks and propagates to the polar region along the inner boundary near the black hole through the Alfvén wave. The jets cannot be cooled through neutrino processes.

4. The quasi-steady disk is not an advection-dominated accretion flow but a neutrino cooling-dominated disk. The accretion time is larger than the cooling time via neutrino. At an inner region ($< 100\text{km}$) of the disk, the profiles of density and temperature are similar to those in Proga et al. (2003).
5. The radial profiles of the density and the temperature of the quasi-steady disk are well described with those of a neutrino cooling dominated disk, or $\rho \sim r^{-51/20}$ and $T \sim r^{-3/10}$, in which the gas pressure is dominated over the other pressure. These profiles are rather different from those of ADAF, or $\rho \sim r^{-3/2}$ and $T \sim r^{-5/8}$.
6. Mass accretion rates in the quasi-steady disks are greater than $0.01M_{\odot}\text{s}^{-1}$ with large fluctuations. A small fraction of rest-mass energy is liberated through neutrino emitted from the dense part of the quasi-steady disks, which hardly trap neutrino. The neutrino luminosity stays at a constant level of $< 8 \times 10^{51}\text{ergs s}^{-1}$, which is much smaller than those from a SN and in the previous work (Proga et al. 2003).

The mass and total energy of the jets are $0.0018\text{--}0.037 M_{\odot}$ and $5 \times 10^{49} - 5 \times 10^{50}$ ergs, respectively (Table 2). The jets are too heavy and weak to produce a relativistic fireball, or GRB, whose baryon mass and isotopic energy are required to be $\leq 10^{-4} - 10^{-5} M_{\odot}$ and 10^{51} ergs (e.g., Hurley, Sari & Djorgovski 2004). The jets are baryon-rich and cannot be accelerated to a relativistic velocity, or failed GRB, as in the previous works (Proga et al. 2003; Mizuno et.al 2004a,b). However, after the generation of the jets, the polar region near the black hole becomes baryon-poor and large magnetic field. If we continue to perform simulations, a baryon-poor outflow may be produced from the region. We need much longer simulations and thus much wider computational domain to examine the ejection of these multipul jets.

Although no jet appear in R8 and S8 during the computation, a jet could be originated near the black hole if the computation is performed for a longer time. However, at the end of the computation, the density sharply drops near the outer boundary because material inside the computational domain begins to be consumed to infall the black hole, whose mass attains $2.64M_{\odot}$ for R8. In order to perform calculation for a longer time to investigate whether a jet can be produced or not, we need a larger computational domain. Our numerical grid cannot resolve the fastest growing mode of MRI for R8 and S8. Therefore, we need longer

calculation with a larger computational domain and finer numerical grids to examine the jet generation in R8 and S8. This is our future task.

The density and temperature of jets can attain so high that material in the jets is in nuclear statistical equilibrium. For relatively low density jets, the composition is protons and neutrons near the black hole. As jets propagate along the rotational axis to decrease the density and temperature, alpha-rich freezeout operates inside the jets, which is mainly composed of ^4He and ^{56}Ni . On the other hands, for dense jets, such as the jet in R12, the jets can be neutron-rich due to electron capture on protons, as suggested by one-dimensional calculations for collapsar disk and jets (Fujimoto et al. 2004, 2005). Consequently, r -process can operate in such dense jets and neutron-rich heavy nuclei, up to 3rd-peak elements can produce inside the jets (Fujimoto et al. in preparation).

This work was supported in part by the Japan Society for Promotion of Science(JSPS) Research Fellowships (K.K.), Grants-in-Aid for the Scientific Research from the Ministry of Education, Science and Culture of Japan (No.S14102004, No.14079202, No.17540267), and Grant-in-Aid for the 21st century COE program “Holistic Research and Education Center for Physics of Self-organizing Systems”. We are grateful to K. Arai for his carefully reading the manuscript and giving useful comments.

REFERENCES

- Akiyama, S., Wheeler, J. C., Meier, D. L., & Lichtenstadt, I. 2003, *ApJ*, 584, 954
- Aloy, M. A., Müller, E., Ibáñez, J. M., Martí, J. M., & MacFadyen, A. 2000, *ApJ*, 531, L119
- Aloy, M.-Á., Martí, J.-M., Gómez, J.-L., Agudo, I., Müller, E., & Ibáñez, J.-M. 2003, *ApJ*, 585, L109
- Balbus, S. A. & Hawley, J. F. 1998, *Rev. Mod. Phys.*, 70, 1
- Blinnikov, S. I., Dunina-Barkovskaya, N. V., & Nadyozhin, D. K. 1996, *ApJS*, 106, 171
- Blondin, J. M., Mezzacappa, A., & DeMarino, C. 2003, *ApJ*, 584, 971
- Di Matteo, T., Perna, R., & Narayan, R. 2002, *ApJ*, 579, 706
- Fryer, C. L., & Heger, A. 2005, *ApJ*, 623, 302
- Fujimoto, S., Arai, K., Matsuba, R., Hashimoto, M., Koike, O., & Mineshige, S. 2001, *PASJ*, 53, 509

- Fujimoto, S., Hashimoto, M., Arai, K., & Matsuba, R. 2004, *ApJ*, 614, 817
- Fujimoto, S., Hashimoto, M., Arai, K., & Matsuba, R. 2005, *Nucl. Phys. A* 758, 47
- Galama, T., et al. 1998, *Nature*, 395, 670
- Hashimoto, M. 1995, *Prog. Theor. Phys.* 94 663.
- Heger, A., Fryer, C. L., Woosley, S. E., Langer, N., & Hartmann, D. H. 2003, *ApJ*, 591, 288
- Heger, A., Woosley, S. E., Langer, N., & Spruit, H. C. in *IAU Symp.* 215, *Stellar Rotation*, in press (astro-ph/0301374)
- Heger, A., Woosley, S. E., & Spruit, H. C. 2005, *ApJ*, 626, 350
- Hjorth, J., et al. 2003, *Nature*, 423, 847
- Hurley K., Sari R. & Djorgovski S.G., 2004, to appear in *Compact Stellar X-ray Sources*, eds. W.H.G. Lewin, M. van der Klis, Cambridge Univ. Press (astro-ph/0211620)
- Kohri, K., & Mineshige, S. 2002, *ApJ*, 577, 311
- Kotake, K., Sawai, H., Yamada, S., & Sato, K. 2004, *ApJ*, 608, 391
- Kotake, K., Yamada, S., Sato, K., Sumiyoshi, K., Ono, H., & Suzuki, H. 2004, *Phys. Rev. D.*, 69, 124004
- Kotake, K., Yamada, S., & Sato, K. 2005, *ApJ*, 618, 474
- Lee, W. H., & Ramirez-Ruiz, E. 2005, preprint (astro-ph/0509307)
- Liebendörfer, M., Mezzacappa, A., Thielemann, F., Messer, O. E., Hix, W. R., & Bruenn, S. W. 2001, *Phys. Rev. D*, 63, 103004
- MacFadyen, A. I., & Woosley, S. E. 1999, *ApJ*, 524, 262 (MW99)
- MacFadyen, A. I., Woosley, S. E., & Heger, A. 2001, *ApJ*, 550, 410
- Maeder, A., & Meynet, G. 2004, *A&A*, 422, 225
- Masada, Y. 2005, private communication.
- Mizuno, Y., Yamada, S., Koide, S., & Shibata, K. 2004a, *ApJ*, 606, 395
- Mizuno, Y., Yamada, S., Koide, S., & Shibata, K. 2004b, *ApJ*, 615, 389

- Narayan, R., Piran, T., & Kumar, P. 2001, *ApJ*, 557, 949
- Paczynski, B., & Wiita, P. J. 1980, *A&A*, 88, 23
- Petrovic, J., Langer, N., Yoon, S.-C., & Heger, A. 2005, *A&A*, 435, 247
- Popham, R., Woosley, S. E., & Fryer, C. 1999, *ApJ*, 518, 356
- Proga, D., MacFadyen, A. I., Armitage, P. J., & Begelman, M.,C. 2003, *ApJ*, 599, 5
- Sekiguchi, Y., & Shibata, M. 2004, *Phys. Rev. D*, 70, 084005
- Sekiguchi, Y., & Shibata, M. 2005, *Phys. Rev. D*, 71, 084013
- Setiawan, S., Ruffert, M., & Janka, H.-T. 2004, *MNRAS*, 352, 753
- Shakura, N. I., & Sunyaev, R. A. 1973, *A&A*, 24, 337
- Shen, H., Toki, H., Oyamatsu, K., & Sumiyoshi, K. 1998, *Nucl. Phys. A.*, 637, 435
- Spruit, H. C. 2002, *A&A*, 381, 923
- Stone, J. M., & Norman, M. L. 1992, *ApJS*, 80, 791
- Stone, J. M., & Pringle, J. E. 2001, *MNRAS*, 322, 461
- Surman, R., & McLaughlin, G. C. 2003, *ApJ*, 603, 611
- Takiwaki, T., Kotake, K., Nagataki, S., & Sato, K. 2004, *ApJ*, 616, 1086
- Wheeler, J. C., Meier, D. L., & Wilson, J. R. 2002, *ApJ*, 568, 807
- Woosley, S. E., & Baron, E. 1992, *ApJ*, 391, 221
- Woosley, S. E. 1993, *ApJ*, 405, 273
- Woosley, S. E., & Weaver, T. A. 1995, *ApJS*, 101, 181
- Yamada, S., & Sawai, H., 2004, *ApJ*, 608, 907
- Yamada, S., Kotake, K., & Yamasaki, T. 2004, *New. J. Phys.*, 6, 79
- Yokosawa, M., Uematsu, S., & Abe J. 2004, preprint (astro-ph/0412558)
- Zeh, A., Klose, S., & Hartmann, D. H. 2004, *ApJ*, 609, 952
- Zhang, W., Woosley, S. E., & MacFadyen, A. I. 2003, *ApJ*, 586, 356

Table 1. Parameters and features of models.

model	B_0	Ω_0	R_0	t_f	$ T/W _0$	$ T/W _f$	$ E_m/W _0$	$ E_m/W _f$	M_f
R8	10^8	10	1000	4.52	1.86	0.27	1.35e-8	2.99e-3	2.46
R10	10^{10}	10	1000	2.62	1.86	3.18e-3	1.35e-4	3.70e-4	2.63
R12	10^{12}	10	1000	0.36	1.86	8.48e-2	1.35	4.68e-2	1.88
S8	10^8	0.5	5000	3.87	0.11	0.20	1.35e-8	6.03e-3	3.55
S10	10^{10}	0.5	5000	1.34	0.11	3.98e-3	1.35e-4	9.88e-4	3.16
S12	10^{12}	0.5	5000	0.28	0.11	3.82e-2	1.35	1.01e-2	2.21

Note. — Model parameters, B_0 , Ω_0 , and R_0 , are shown in units of G, rad s^{-1} , and km, respectively. The calculations are stopped at the time t_f , when the mass of the central black hole is M_f in units of M_\odot . The ratios $|T/W|_0$, $|T/W|_f$, $|E_m/W|_0$ and $|E_m/W|_f$ are expressed in percentage.

Table 2. Jet properties

model	t_{jet}	M_{ej}	$(E_m)_{\text{ej}}$	$(E_k)_{\text{ej}}$	$(E_i)_{\text{ej}}$
R10	2.58	0.0010	2.89e-4	0.0274	0.0840
R12	0.20	0.083	0.097	4.58	2.79
S10	1.30	0.0053	0.045	0.138	0.606
S12	0.25	0.033	0.014	3.57	5.27

Note. — Jets are passed through 1000km at the time t_{jet} (s) from the central black hole. Ejected mass via jets, M_{ej} , is in units of M_\odot . Magnetic, kinetic, and internal energies carried away via jets, $(E_m)_{\text{ej}}$, $(E_k)_{\text{ej}}$, and $(E_i)_{\text{ej}}$, are expressed in 10^{50}erg .

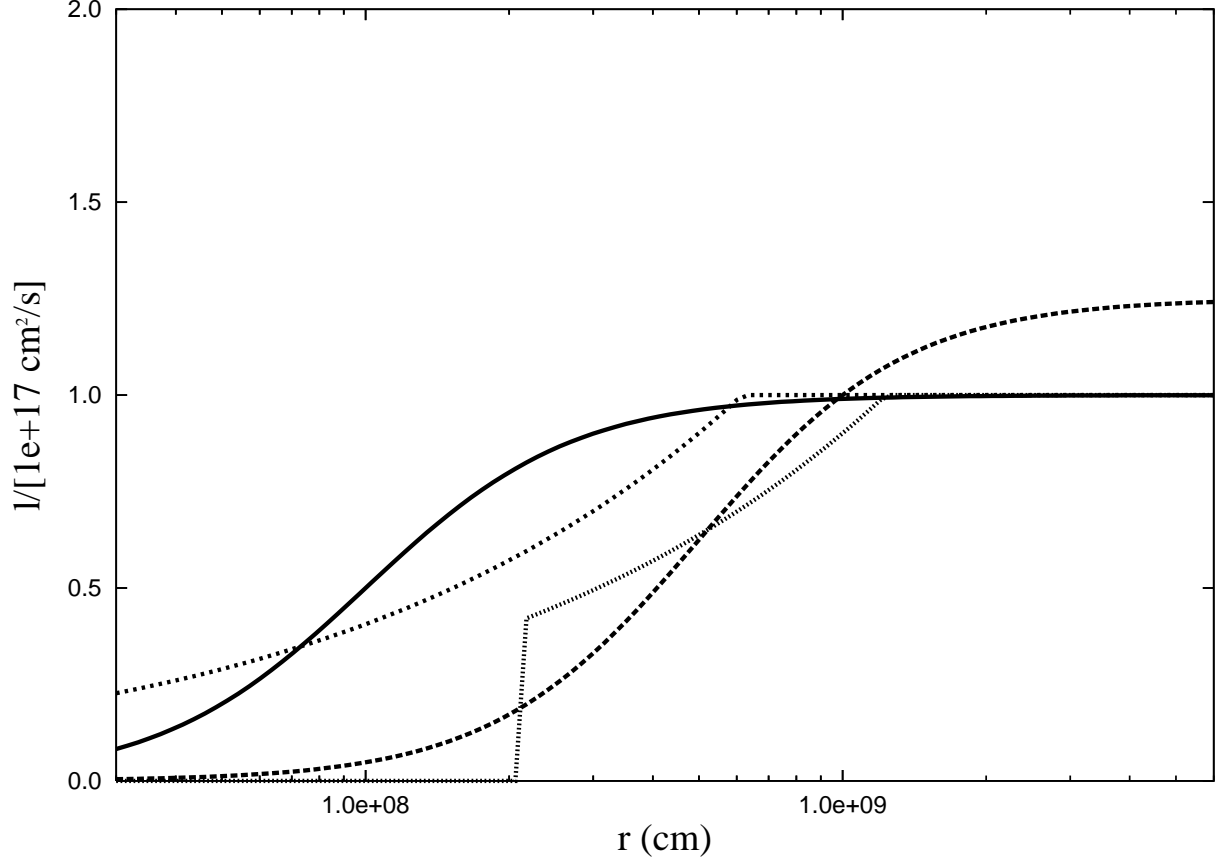


Fig. 1.— Initial angular momentum distribution inside the collapsing star at the equatorial plane. The solid, dashed, dotted, and dash-dotted lines represent distributions for rapidly rotating core ($R_0 = 1000\text{km}$ and $\Omega_0 = 10 \text{ rad s}^{-1}$) and for slowly rotating core ($R_0 = 5000\text{km}$ and $\Omega_0 = 0.5 \text{ rad s}^{-1}$), those of MacFadyen & Woosley (1999) and Proga et al. (2003), respectively.

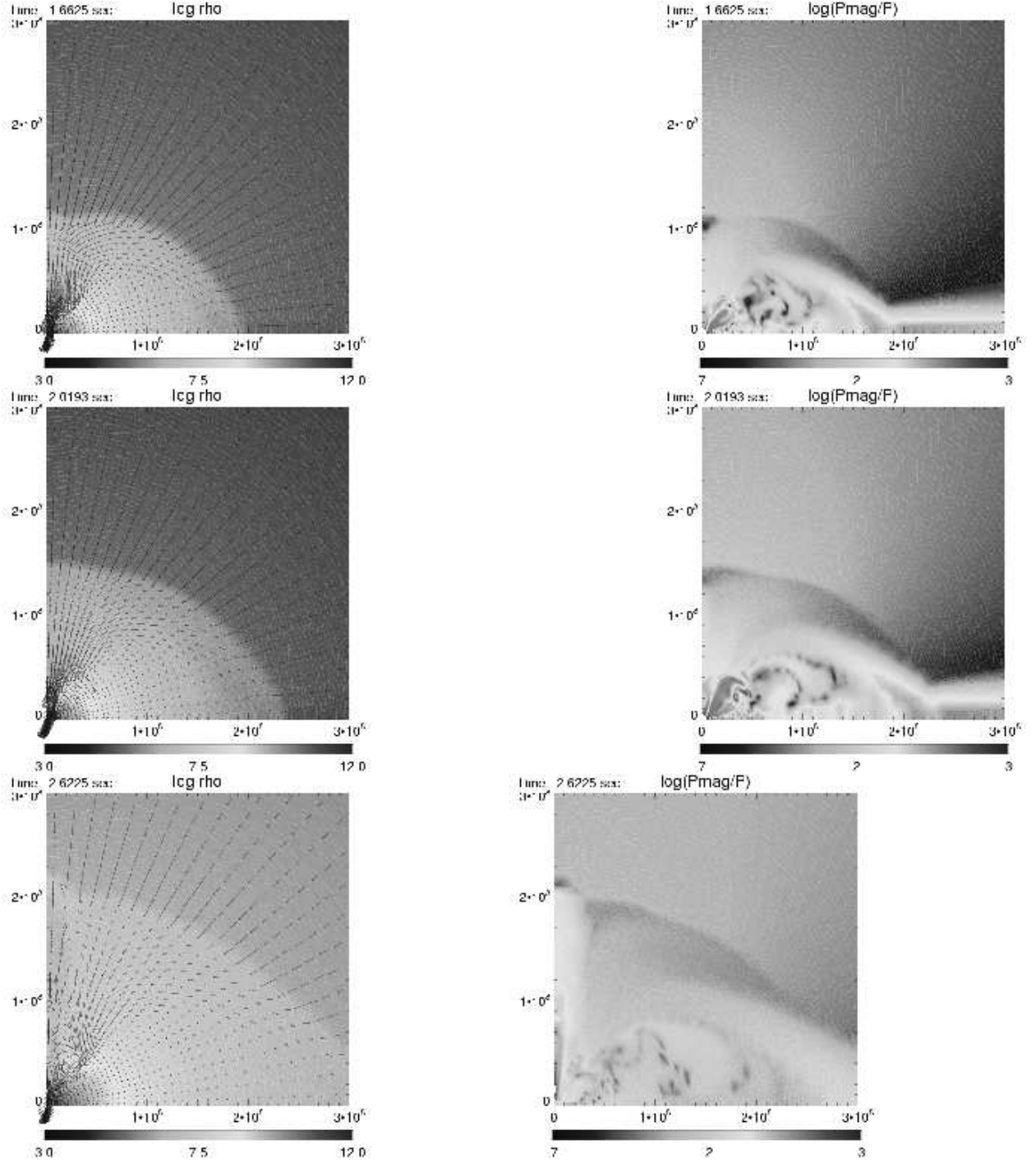


Fig. 2.— Contours of the density (left panels) and the ratio of P_{mag} to the pressure (right panels) for R10 at $t = 1.6625$, 2.0193 , and, 2.6225 s (from top to bottom).

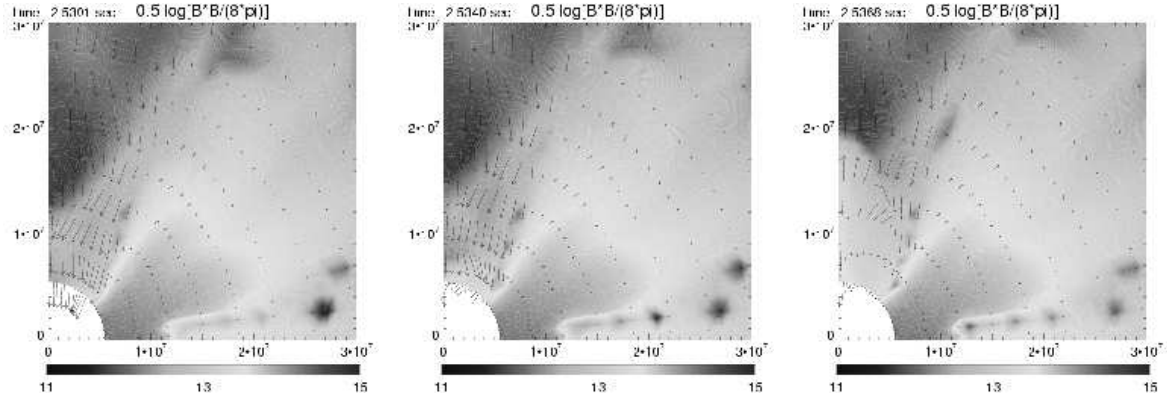


Fig. 3.— Contours of P_{mag} for R10 at $t = 2.5301, 2.5340,$ and 2.5368 s (from left to right). Magnetic field enhanced inside the disk propagates along the inner boundary (left and center panels). Jets are driven by the magnetic pressure near the boundary (center panel) and propagates along the rotational axis (right panel).

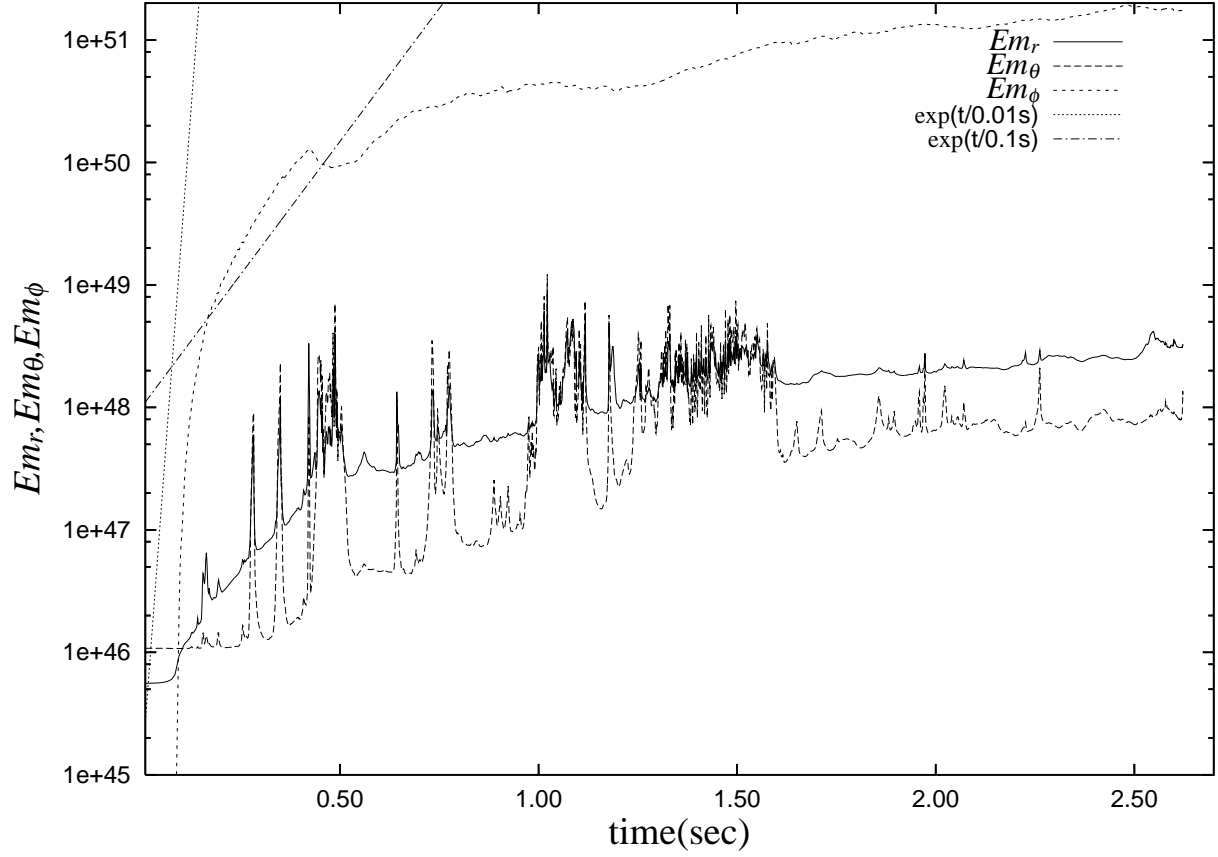


Fig. 4.— Time evolution of the magnetic energies integrated over the entire computational domain, defined as $E_{m,i} = \int (B_i^2/8\pi) dV$ ($i = r, \theta, \phi$). The solid, dashed, and dotted lines represent $E_{m,r}$, $E_{m,\theta}$, and $E_{m,\phi}$, respectively.

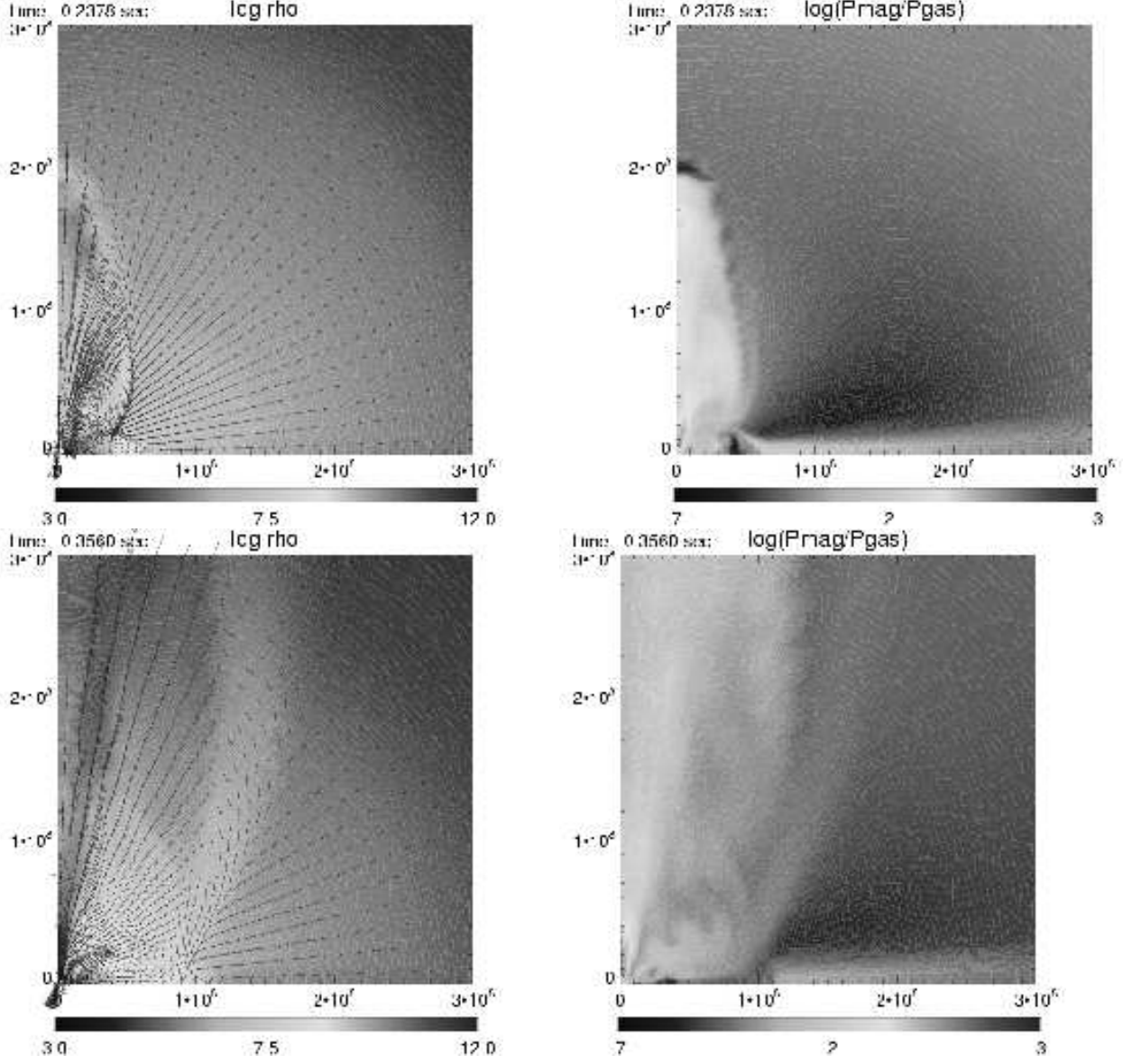


Fig. 5.— Contours of density (left panels) and the ratio of P_{mag} to the pressure (right panels) for R12 at $t = 0.2378$ and 0.3560 s.

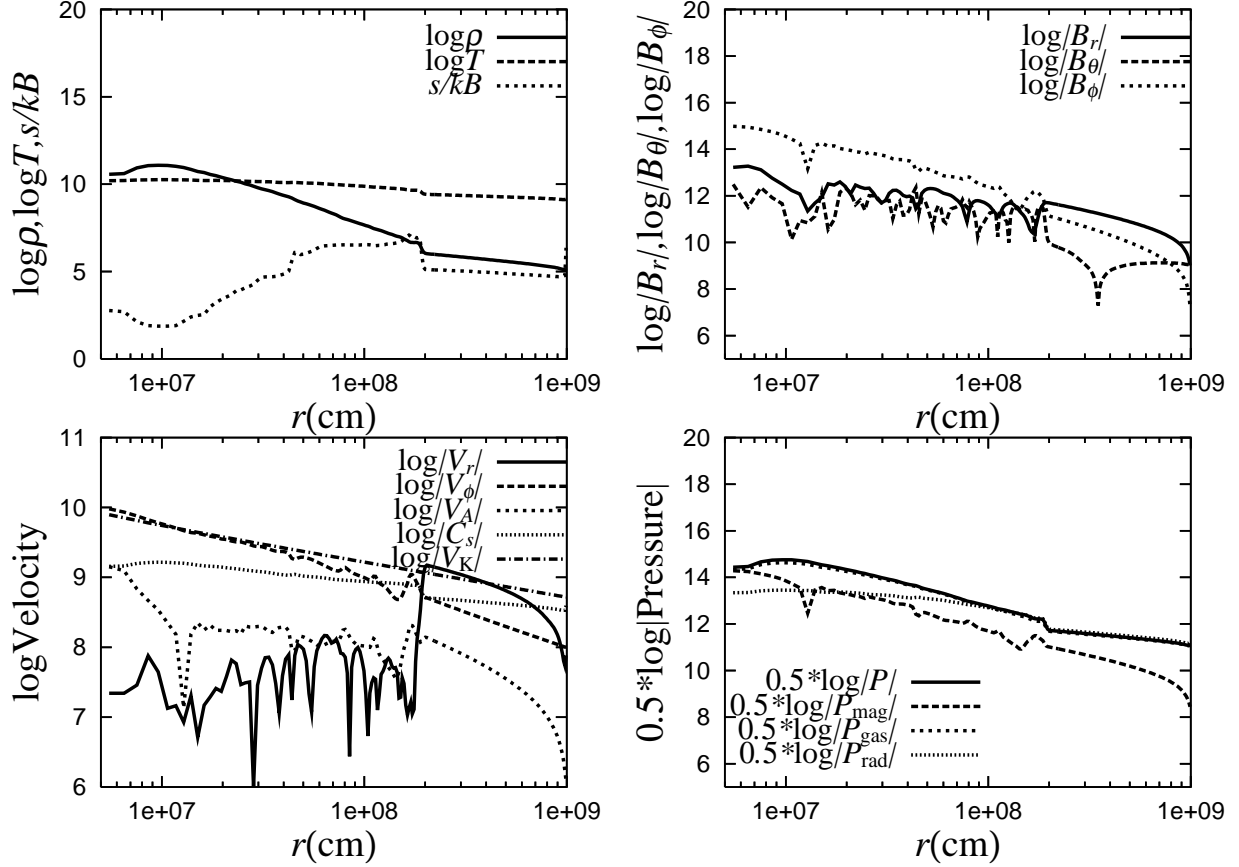


Fig. 6.— Physical quantities near the equatorial plane ($\theta = 88.1^\circ$) for R10 at 1.6625 s. The top left panel plots the logarithmic density in g cm^{-3} (solid line), logarithmic temperature in K (dotted line), and entropy per baryon in the Boltzmann constant (dashed line). The top right panel plots logarithmic magnetic fields. Solid, dotted, and dashed lines represent the radial, azimuthal, and toroidal components of the magnetic field in units of G, respectively. The bottom left panel plots logarithmic velocities in cm s^{-1} ; the radial velocity (solid line), the angular velocity (dotted line), the Alfvén speed (dashed line), the sound speed (solid-dotted line), and the Keplerian velocity around a $2M_\odot$ black hole (solid-triple dotted line). The bottom right panel plots logarithmic pressure in ergs cm^{-3} .

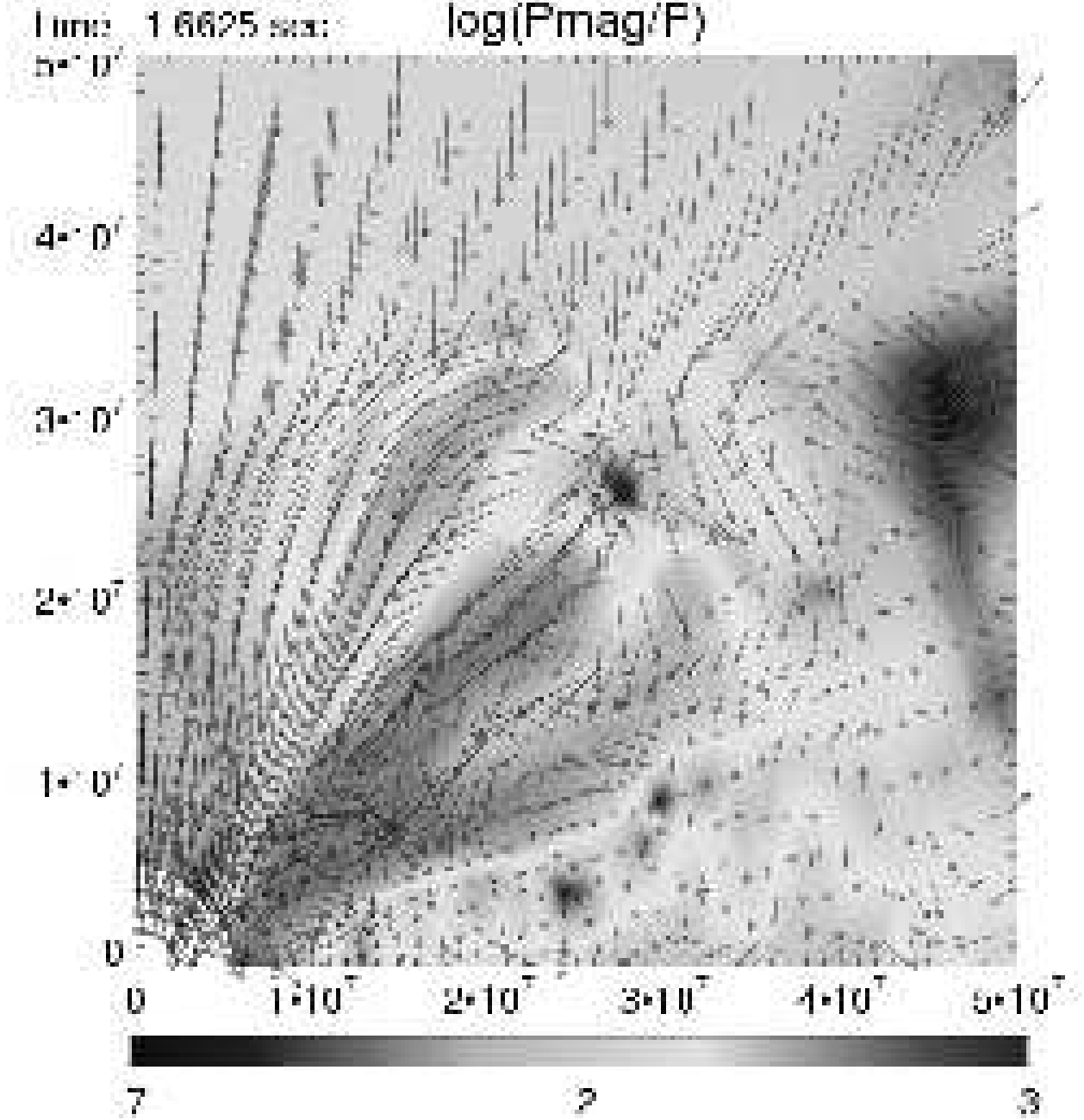


Fig. 7.— Contours of the ratio of P_{mag} to the pressure at an inner region ($500 \text{ km} \times 500 \text{ km}$) of an accretion disk for R10 at $t = 1.6625 \text{ s}$.

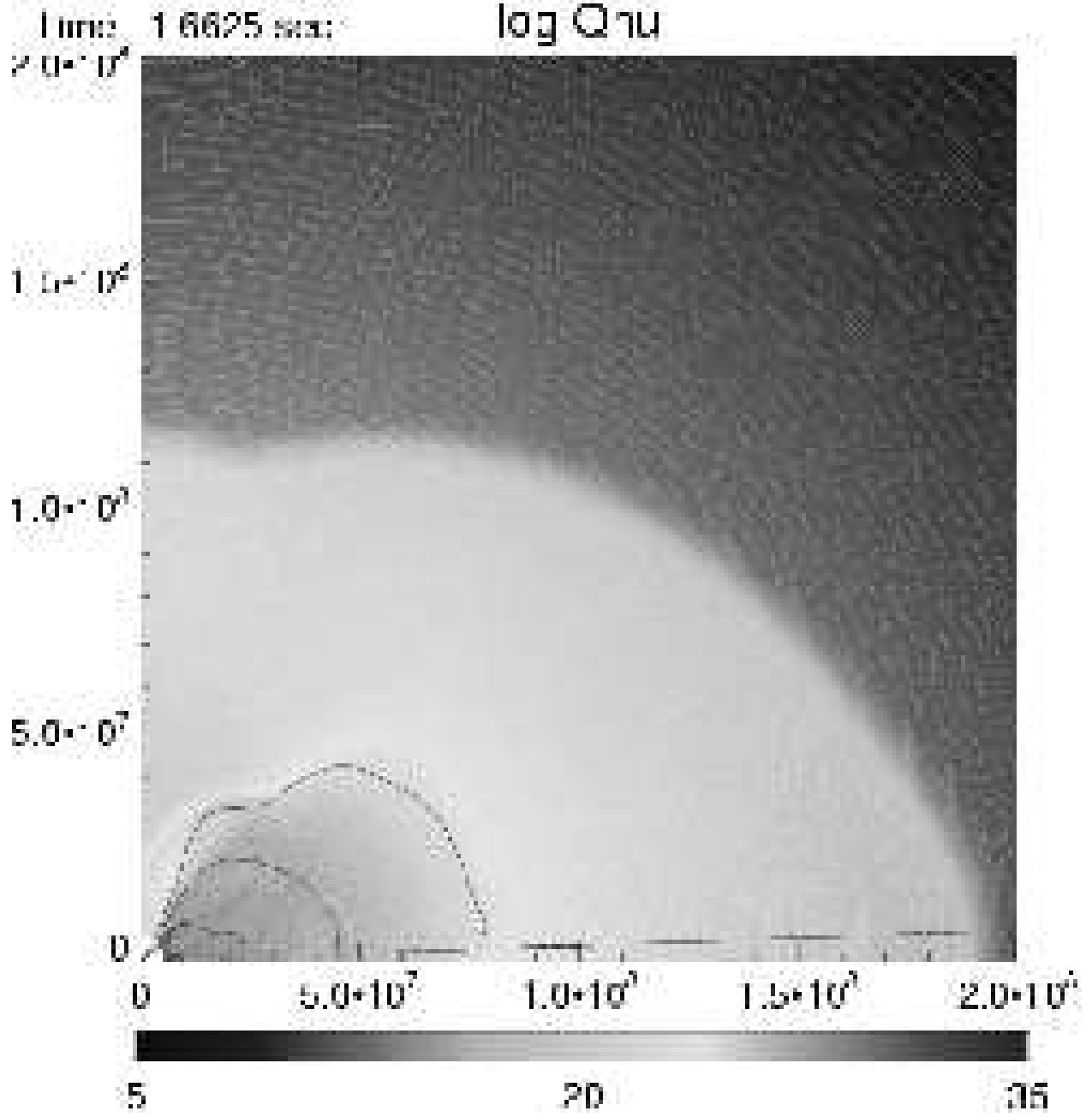


Fig. 8.— Contour of logarithmic specific neutrino cooling rate in units of ergs s $^{-1}$ cm $^{-3}$ for R10 at 1.6625 s. Density contours of 10^8 , 10^9 , 10^{10} , and 10^{11} g cm $^{-3}$ are also shown.

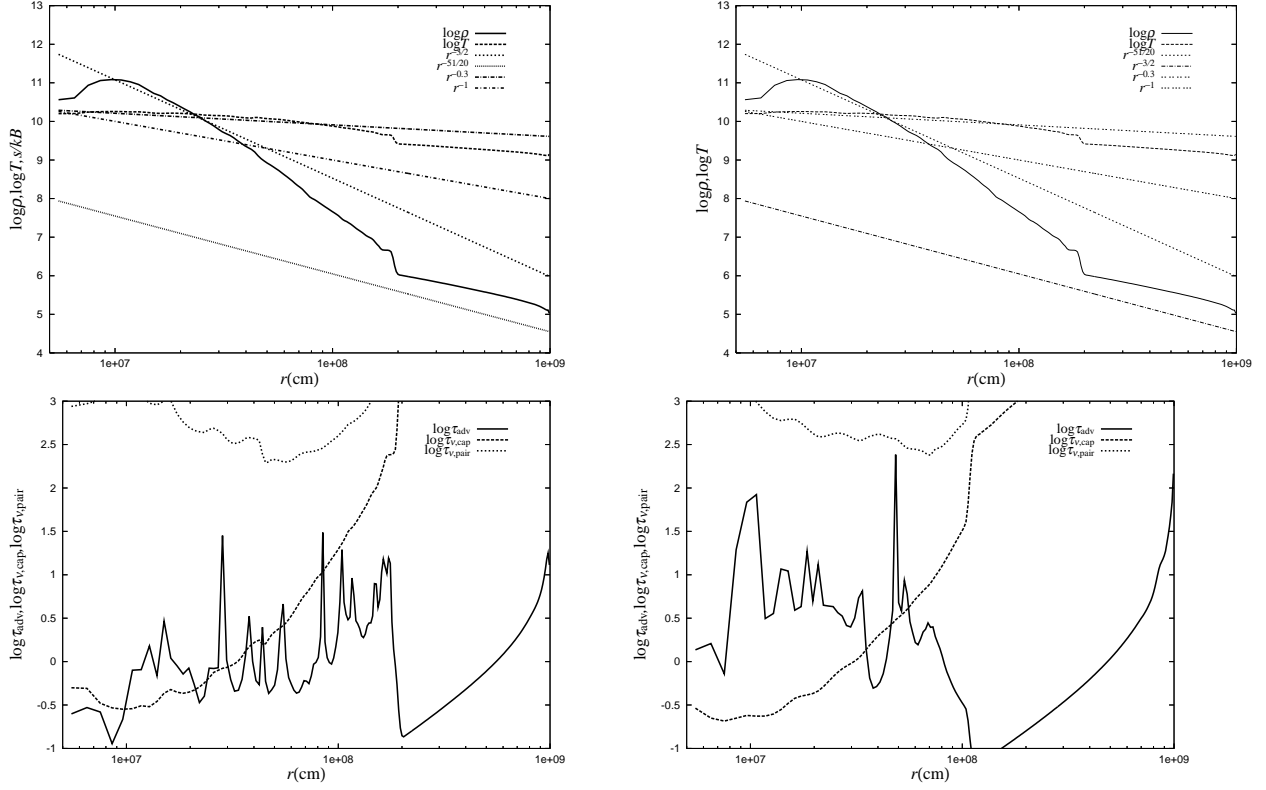


Fig. 9.— Radial profiles of the density and temperature in our models and those of ADAF and NDAF (top panels), and the accretion timescale and the neutrino cooling timescale (bottom panels) near the equatorial plane ($\theta = 88.1^\circ$). The top left panel plots the radial profiles of density (solid line) and temperature (dotted line) for R10 at 1.6635 s. Dotted and double dashed lines are scaled density and temperature profiles of NDAF, respectively, and triple dashed and dot dashed lines are those of ADAF. At an inner region, the radial profiles are well described those of NDAF. The top right panel is same as the top left panel but for R8 at 4.0000 s. The bottom left panel plots accretion timescale (solid line) and neutrino cooling timescale through pair capture (dashed line) and pair annihilation (dotted line) for R10 at 1.6635 s. The top right panel is same as the bottom left panel but for R8 at 4.0000 s.

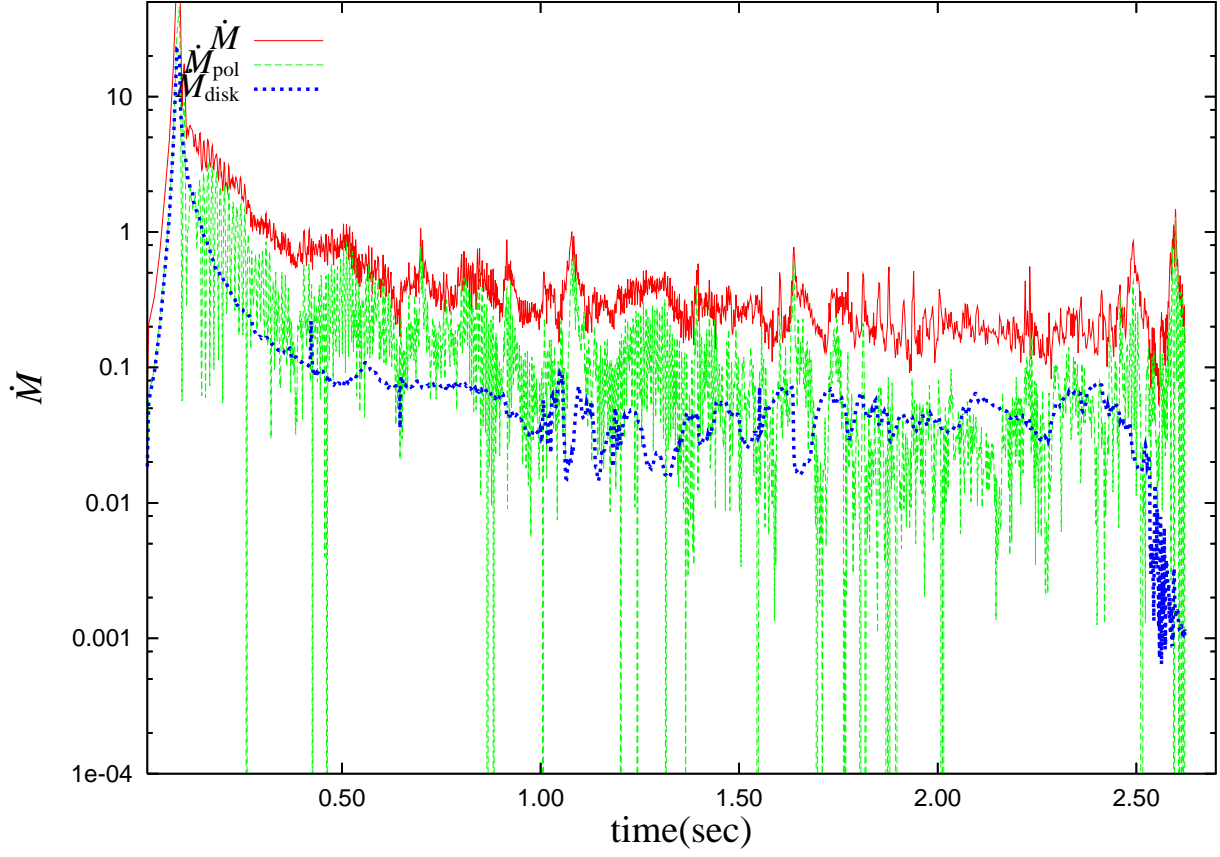


Fig. 10.— Time evolution of the accretion rates. The solid, dashed, and dotted lines represent the rate through the inner boundary at 50km, \dot{M} , the rate through parts of the boundary ($\theta \leq 20^\circ$), \dot{M}_{pol} the rate through parts of the boundary ($\theta \geq 50^\circ$), \dot{M}_{disk} , respectively. All rates are in units of $M_\odot \text{ s}^{-1}$.

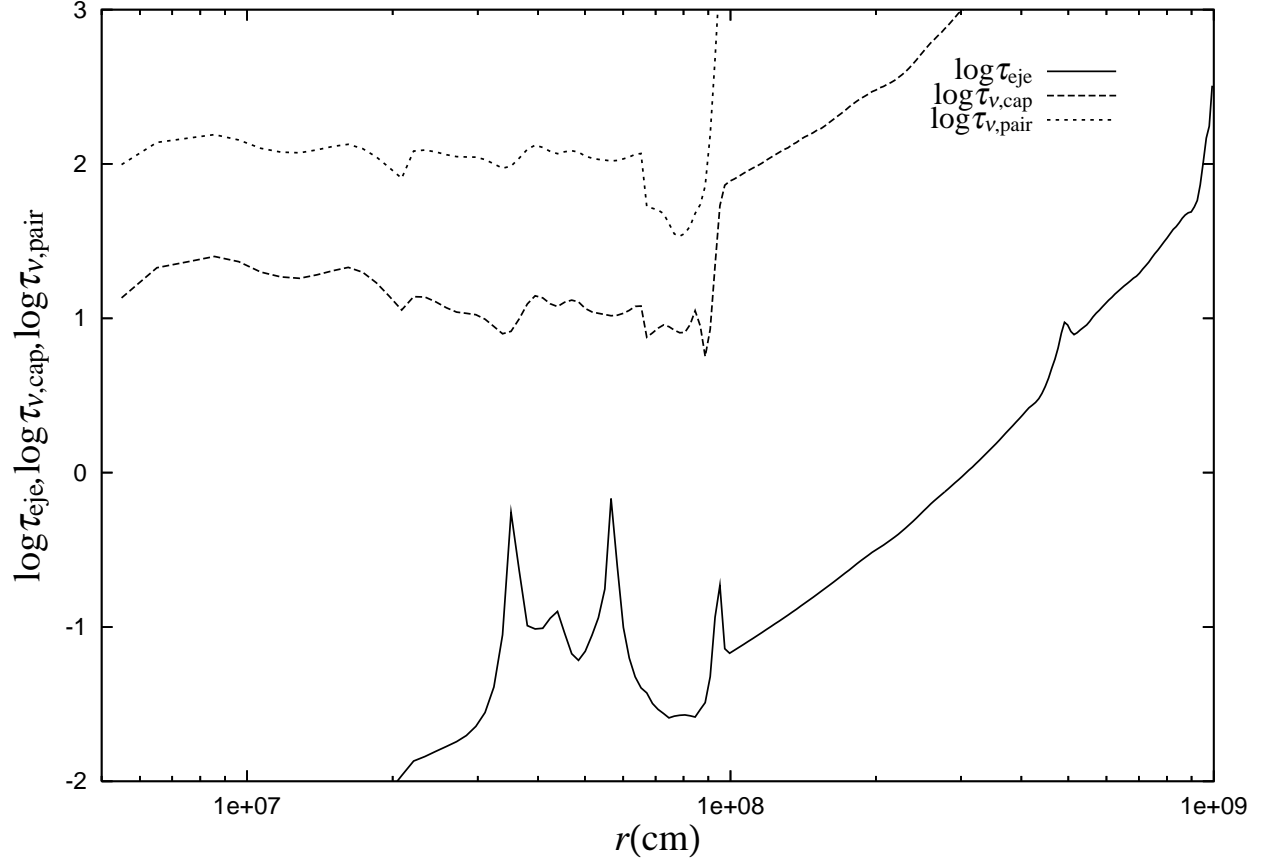


Fig. 11.— Timescale inside a jets for R12 at 0.1997 s. Solid, dashed, and dotted lines are ejection timescale, neutrino cooling timescale through pair capture and that through pair annihilation.

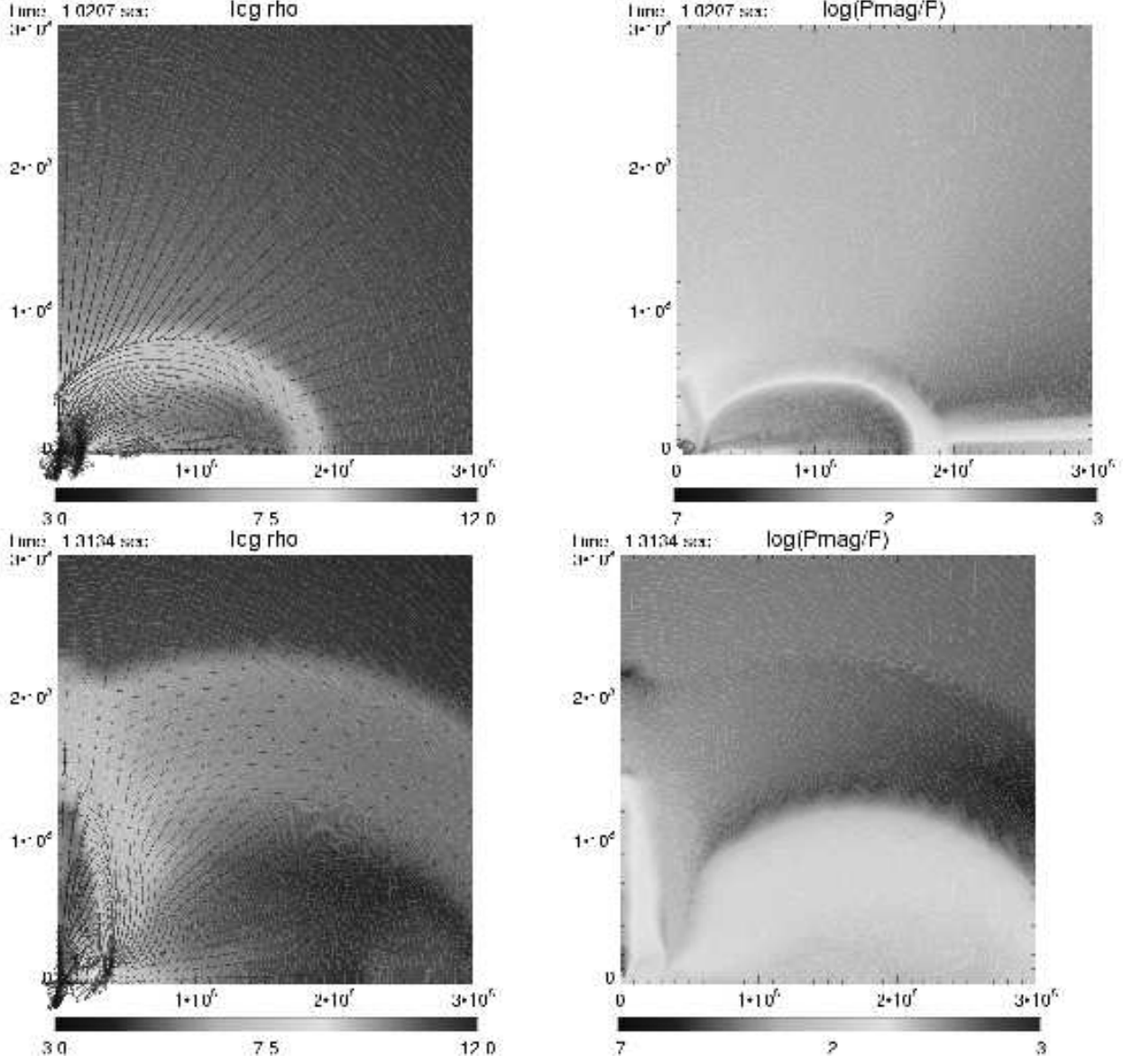


Fig. 12.— Contours of density (left panels) and the ratio of P_{mag} to the pressure (right panels) for S10 at $t = 1.0207$ and 1.3134 s.

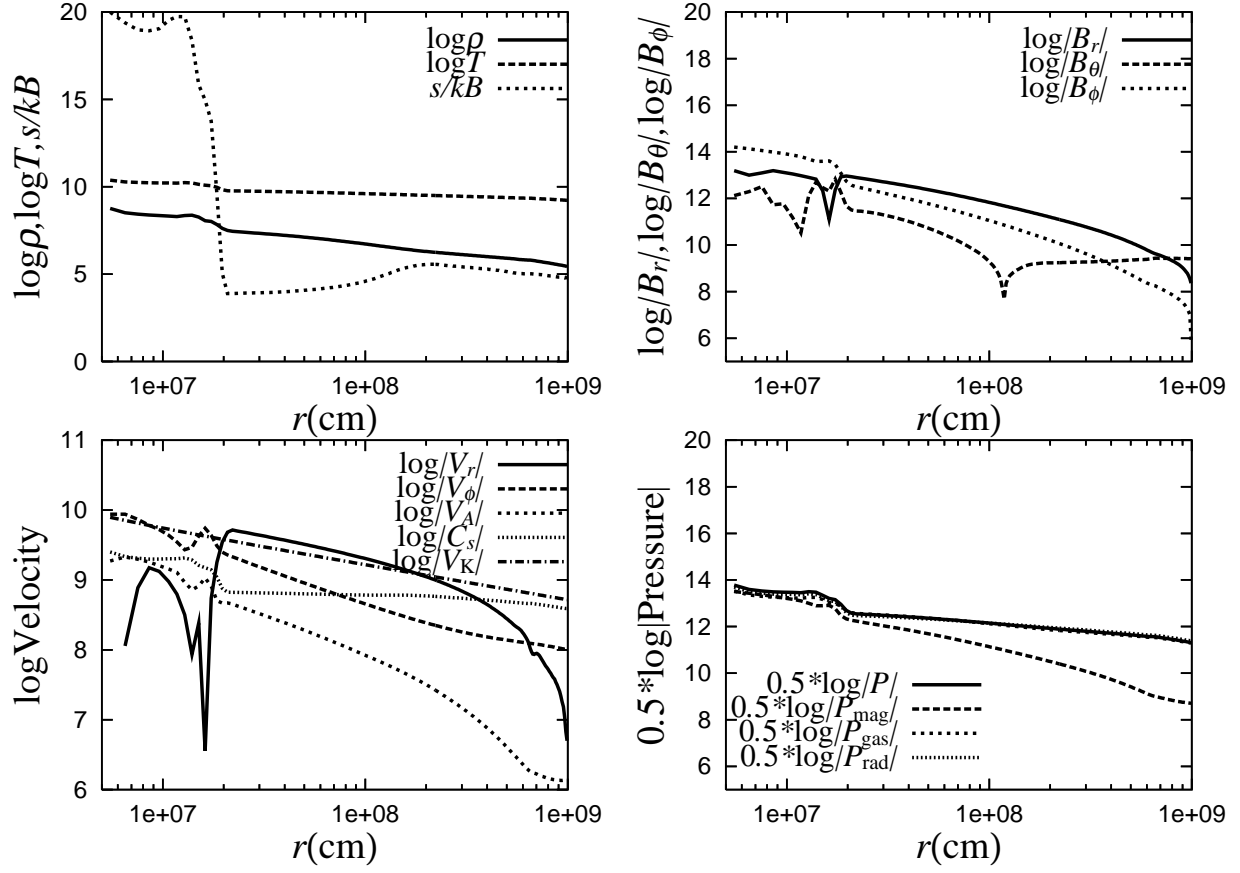


Fig. 13.— Same figure as Figure 6 but for S10 at 0.5676 s.

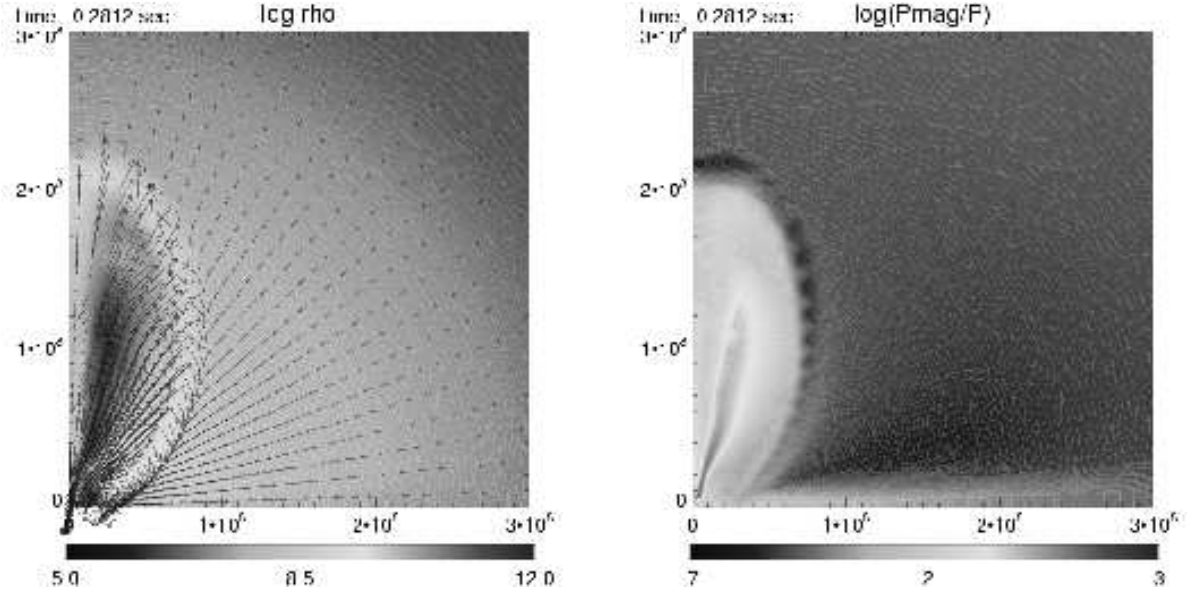


Fig. 14.— Contours of density (left panel) and the ratio of P_{mag} to the pressure (right panel) for S12 at $t = 0.2812$ s.

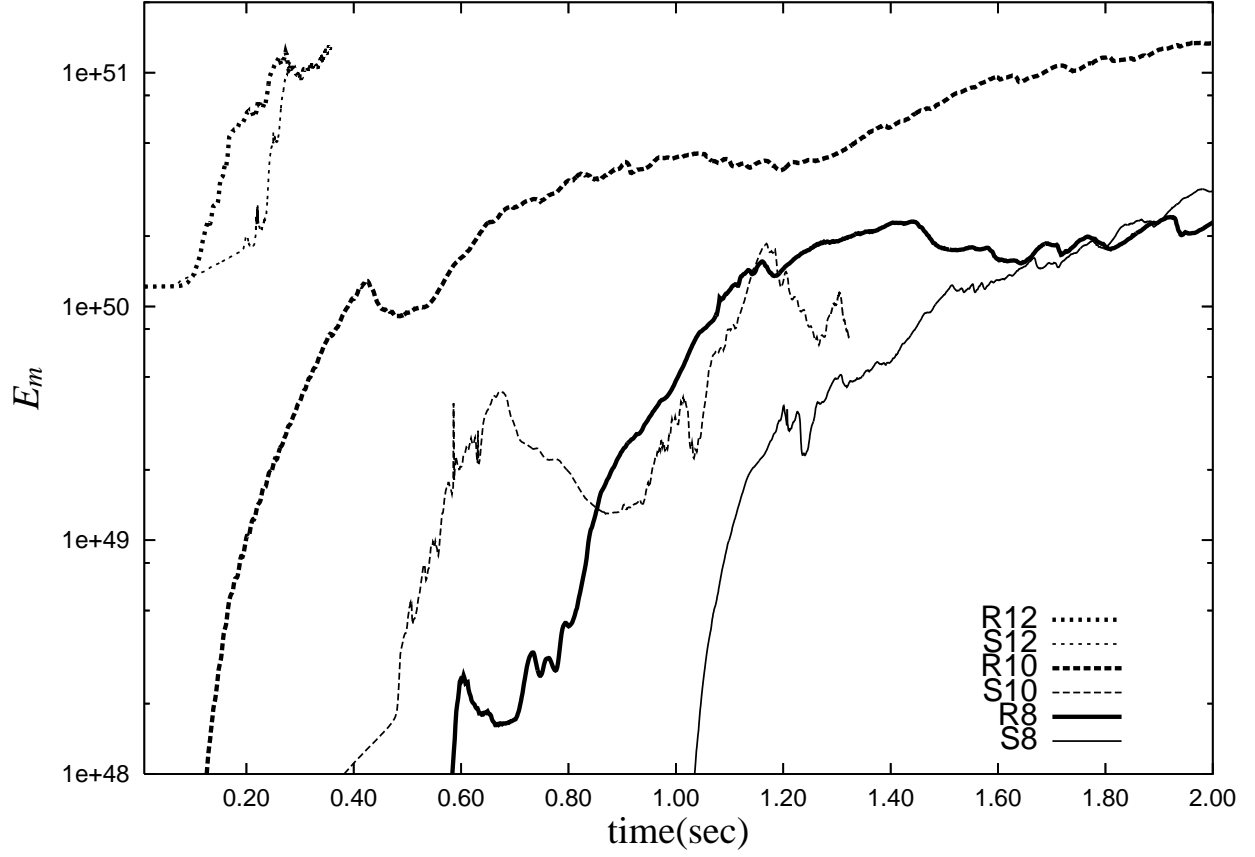


Fig. 15.— Time evolution of the magnetic energy integrated over the computational domain, $E_m = \int (B^2/8\pi) dV$, for all models. The solid, thin-solid, dashed, thin-dashed, dotted, and thin-dotted lines represent the magnetic energy for R8, S8, R10, S10, R12, and S12, respectively.

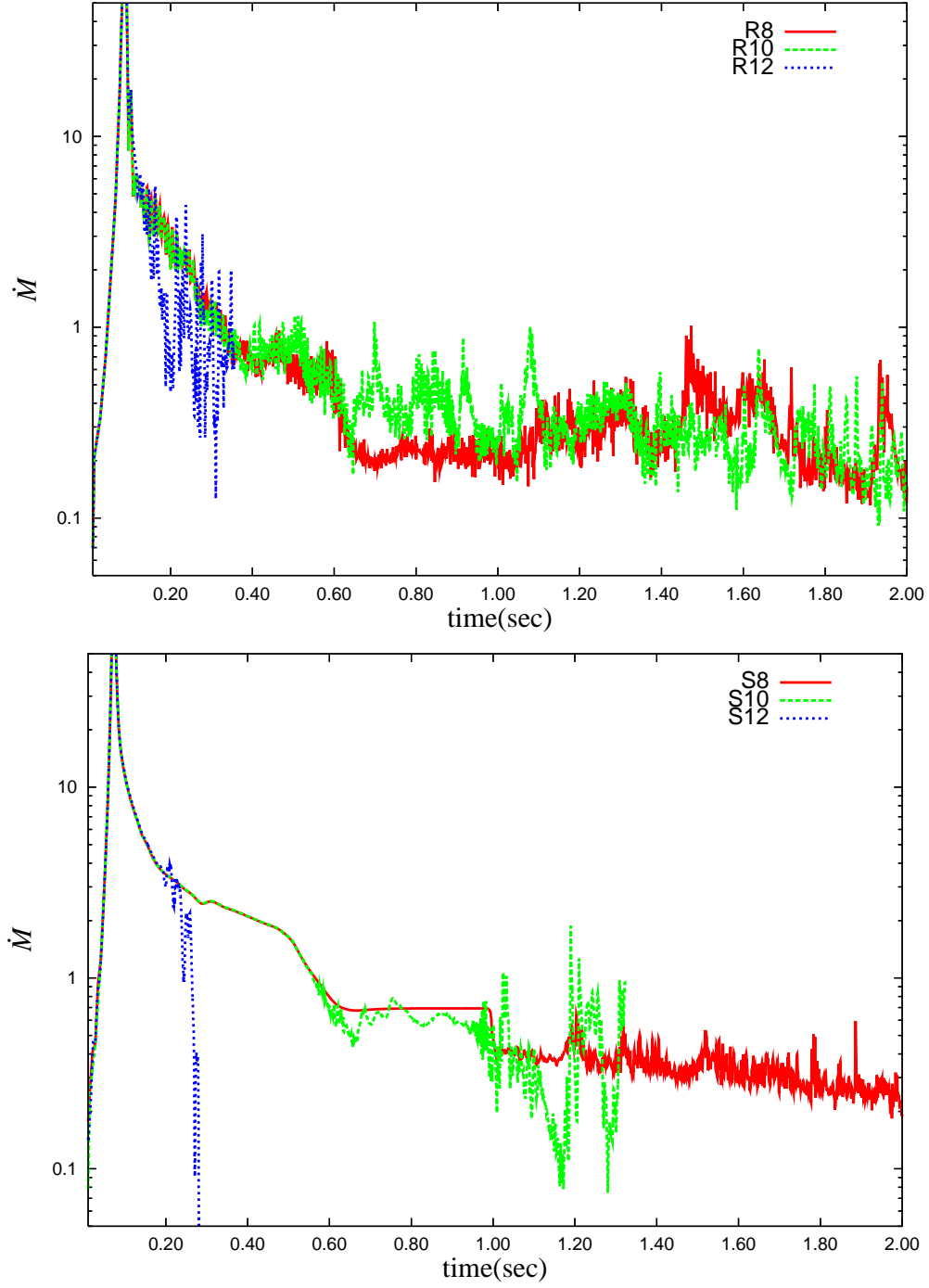


Fig. 16.— Time evolution of the accretion rate through the inner boundary at 50km, \dot{M} , for all models. The solid, dashed, and dotted lines represent the rates for R8, R10, and, R12 (left panel), respectively, and the rates for S8, S10, and, S12 (right panel), respectively.

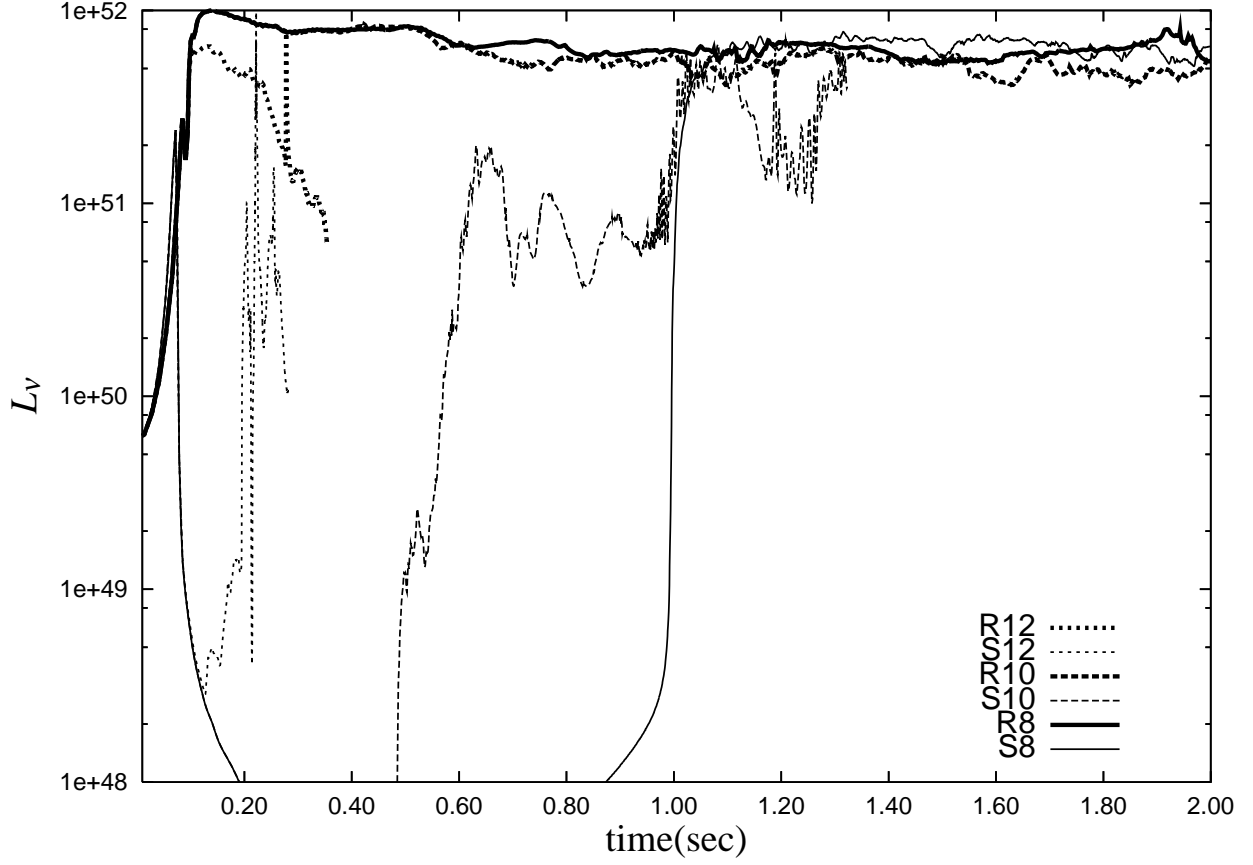


Fig. 17.— Time evolution of the neutrino luminosity integrated over the computational domain, for all models. The solid, thin-solid, dashed, thin-dashed, dotted, and thin-dotted lines represent the neutrino flux for R8, S8, R10, S10, R12, and S12, respectively.

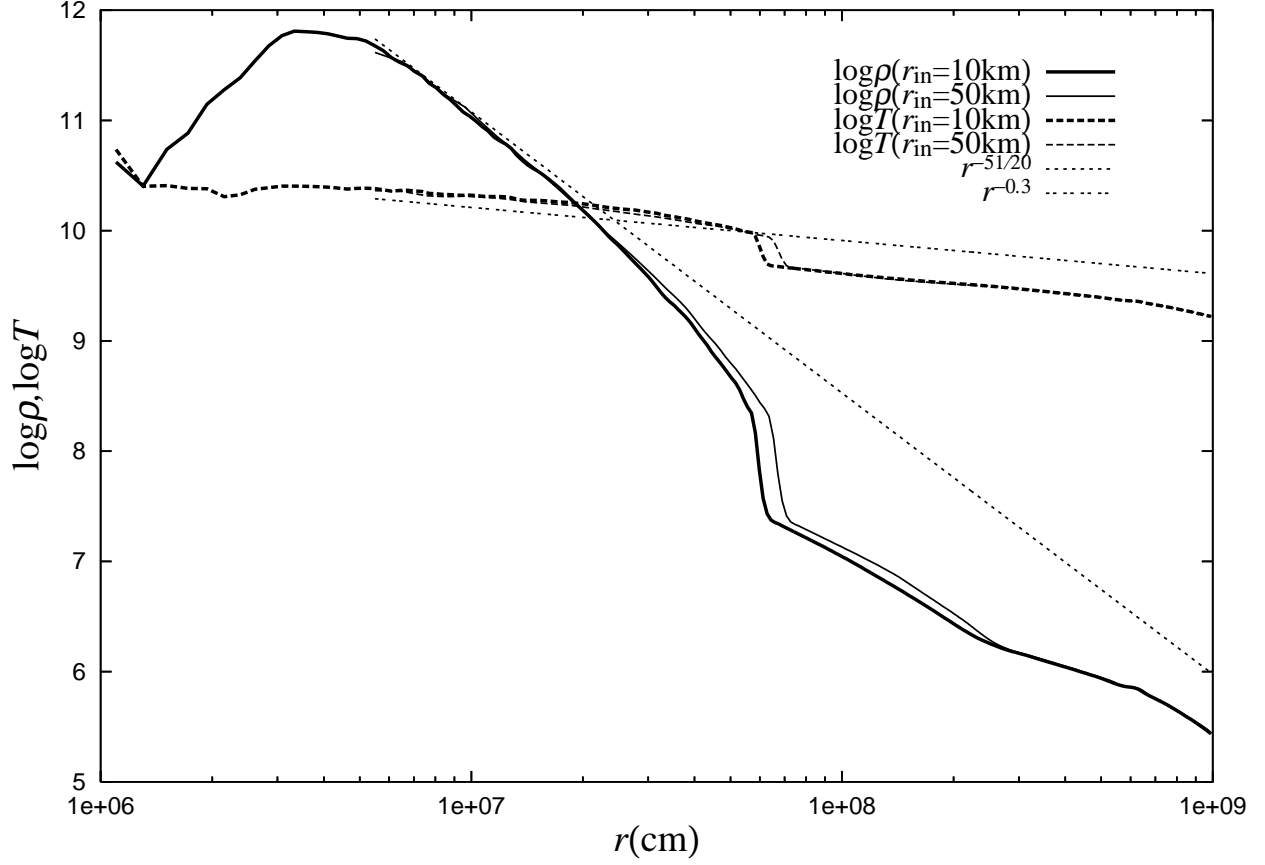


Fig. 18.— Radial profiles of the density (solid lines) and temperature (dotted lines) near the equatorial plane ($\theta = 88.1^\circ$) in R10 at 0.5 s for $r_{\text{in}} = 10$ km and 50 km. Thick and thin lines correspond to the profiles for $r_{\text{in}} = 10$ km and 50 km, respectively. We also plot profiles of the density (dotted line) and temperature (dot dashed lines) of NDAF, as shown in Figure 9. The profiles are independent of the location of the inner boundary.